Two-Point Particle Tracking Microrheology of Nematic Complex Fluids

**Manuel Gómez-González**[*,a] and **Juan C. del Álamo**[a,b]

[a]Mechanical & Aerospace Engineering Department, University of California San Diego, 9500 Gilman Dr., La Jolla, CA 92093-0411, USA.

[b]Institute for Engineering in Medicine, University of California San Diego, 9500 Gilman Dr., La Jolla, CA, 92093-0435, USA

Abstract

Many biological and technological complex fluids exhibit tight microstructural alignment that confers them nematic mechanical properties. Among these we count liquid crystals and biopolymer networks, which are often available in microscopic amounts. However, current microrheological methods cannot measure the directional viscoelastic coefficients that appear in the constitutive relation of nematic complex fluids. This article presents directional two-point particle-tracking microrheology (D2PTM) – a novel microrheology technique to determine these coefficients. We establish the theoretical foundation for D2PTM by analyzing the motion of a probing microscopic particle embedded in a nematic complex fluid, and the mutual hydrodynamic interactions between pairs of distant particles. From this analysis, we generalize the formulation of two-point particle tracking microrheology for nematic complex fluids, and demonstrate that the new formulation provides sufficient information to fully characterize the anisotropic viscoelastic coefficients of such materials. We test D2PTM by simulating the Brownian motion of particles in nematic viscoelastic fluids with prescribed directional frequency-dependent shear moduli, showing that D2PTM accurately recovers the prescribed shear moduli. Furthermore, we experimentally validate D2PTM by applying it to a lyotropic nematic liquid crystal, and demonstrate that this new microrheology method provides results in agreement with dynamic light scattering measurements. Lastly, we illustrate the experimental application of the new technique to characterize nematic F-actin solutions. These experiments constitute the first microrheological measurement of the directional viscoelastic coefficients of an anisotropic soft material.

Graphical Abstract
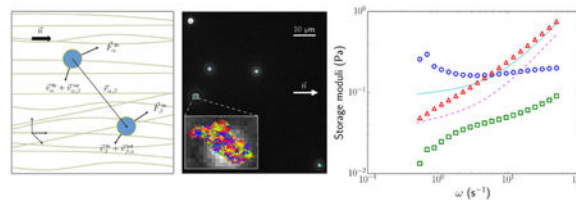
[*]manu@ucsd.edu.

1 Introduction

Particle tracking microrheology (PTM)[1,2] is a useful experimental technique to determine the rheological properties of soft materials that exhibit complex mechanical behaviors and are conveniently available in minute amounts[3,4]. In PTM, submicron-sized particles are embedded in a material sample, excited with a known force, and their displacements are measured as a function of time. From these measurements one can determine the materia's frequency-dependent shear modulus $G(\omega)$. PTM methods can be classified as active or passive depending on the nature of the force that drives particle motion. Active PTM methods apply an external force on the probing particle whereas in passive PTM methods, the embedded microparticles undergo random motion due to thermal and possibly non-thermal fluctuations. Active and passive PTM have been applied to characterize, among other systems, colloidal suspensions[5–7], reconstituted protein gels[8–10], and the cytoplasm of live cells[11–13].

Regardless of the mechanism driving particle motion, a key step of PTM is to connect the measured motion with the underlying rheological properties of the medium. This step requires theoretical knowledge of the relation between the driving force and particle velocity as a function of $G(\omega)$. This relation is usually idealized as Stokesian, *i.e.* $F = 6\pi Ga/\omega$ where a is the particle radius, but there is a number of near field phenomena that generate deviations from Stokesian behavior. Examples of these are partial slip at the particle surface[14], compressibility[15] and electrochemical surface interactions[16]. To eliminate these short-range effects, Crocker *et al.* [17] introduced two-point PTM, which analyzes the cross-correlated motion of pairs of distant particles.

The vast majority of existing PTM protocols (active and passive, single-point and two-point) assume that the probed medium is isotropic. However, there is a substantial number of soft materials that exhibit molecular or supramolecular alignment leading to anisotropic rheology. Anisotropic particle diffusion has been reported in nematic liquid crystals[18,19], reconstituted polymer networks[20,21], and the cytoplasm of cells[12,22–25]. However, there is a lack of microrheological methods to measure the directional viscoelastic coefficients of nematic complex fluids. Previous efforts analyzed particle motion in the principal directions of minimum and maximal motion, and applied Stokes' law in each direction [12,20–22,24,25] This approach provides effective shear moduli that quantify the viscoelastic resistance experienced by the particle in different directions. However, these effective shear moduli do not represent true material viscosities[4], and have been shown to differ substantially from the material viscosity coefficients of the fluid[26]. To address this limitation, Gómez-González and del Álamo[26] studied the flow of a nematic fluid around a sphere using the Leslie-Ericksen constitutive relation. They calculated the drag coefficients of the sphere in the directions parallel and perpendicular to the nematic as functions of the three directional shear moduli of the fluid. They also showed that one-point PTM can only provide up to two independent drag coefficients, which is insufficient to calculate the three shear moduli.

In this paper, we resolve this indetermination by analyzing the cross-correlated motion of pairs of distant spheres in a nematic fluid. Specifically, we derive a closed-form analytical solution for the spheres' mutually induced velocity, *i.e.* the *multiparticle mobility tensor*. We

show that this approach provides three independent equations, so that two-point PTM can be used to determine the rheological properties of nematic fluids that follow the Leslie-Ericksen constitutive relation. The novel directional two-Point PTM (D2PTM) formulation is validated via numerical simulations, as well as experiments in a nematic liquid crystal of known directional viscosity coefficients. Finally, we apply D2PTM to a nematic solution of filamentous actin. These results represent the first direct microrheological measurement of the directional shear moduli of F-actin, enabling future applications of D2PTM to other soft materials.

2 Theoretical Foundation of Directional Two-Point Particle Tracking Microrheology

This section describes the motion of spherical PTM probes embedded in a nematic complex fluid defined by the director $\vec{n}$ (Fig. 1). The drag force experienced by the particles and the interaction between pairs of distant particles (Fig. 2) are calculated. These results are used to develop analysis algorithms for D2PTM.

2.1 Mathematical Formulation

The velocity field of an incompressible complex fluid can be described[27] by the Cauchy's momentum equation

$$\rho \dot{\vec{v}} - \nabla \cdot \bar{\bar{\tau}} = \vec{f}, \quad (1)$$

together with the continuity equation $\nabla \cdot \vec{v} = 0$, where $\vec{f}$ represents the applied external forces, $\vec{v} = \partial_t \vec{u}$ is the velocity field, $\vec{u}$ is the deformation field, ρ is the density and $\bar{\bar{\tau}}$ is the stress tensor. These equations are valid for homogeneous one-component materials, and for semidiluted bio-polymer networks that conform to certain conditions[28], *i.e.* low volume fraction φ of the solute, characteristic length of the displacements a larger than the mesh size ξ, and frequencies $\omega \ll 10^4$ s^{-1}. These conditions are often met in microrheology studies of biological samples such as the eukaryotic cytoplasm ($\varphi \sim 0.01 - 0.02$[29]) and reconstituted bio-polymer networks ($\varphi \sim 0.001 - 0.01$[9,21,30]), where the length scale is the radius of the probing particle $a \gg \xi$ and the frequencies are well below the specified limit[26].

We estimate a Reynolds number $Re = \rho U a/\eta \sim 10^{-6}$ in PTM experiments[26] and thus neglect inertial terms in the equations of motion. We relate the stress and strain ($\bar{\bar{\varepsilon}}$) tensors via a generalization of the Leslie-Ericksen constitutive equations [31–33] in the frequency domain,

$$\widetilde{\tau}_{ij} = -\widetilde{p}\delta_{ij} + \widetilde{\alpha}_1^*(s)\widetilde{n}_k\widetilde{n}_q\widetilde{\varepsilon}_{kq}\widetilde{n}_i\widetilde{n}_j + \widetilde{\alpha}_2^*(s)\widetilde{n}_i\widetilde{N}_j + \widetilde{\alpha}_3^*(s)\widetilde{n}_j\widetilde{N}_i$$
$$+ \widetilde{\alpha}_4^*(s)\widetilde{\varepsilon}_{ij} + \widetilde{\alpha}_5^*(s)\widetilde{n}_i\widetilde{n}_k\widetilde{\varepsilon}_{kj} + \widetilde{\alpha}_6^*(s)\widetilde{n}_j\widetilde{n}_k\widetilde{\varepsilon}_{ki}, \quad (2)$$

where $\widetilde{p}$ represents the pressure, δ the Kronecker delta, $\sim$ indicates Laplace transform, s is the frequency and the subscripts i, j, k and q represent space coordinates. The convention of

summation over the repeated indices k and q holds for this equation. This expression is analogous to the generalized Stokes' formula proposed by Mason and Weitz[1]. It depends on six complex viscoelasticity coefficients $\tilde{\alpha}_k^*(s)$, the director of the nematic $\tilde{n}_i$, and the rate of change of the director with respect to the background fluid, $\tilde{N}_i$. The viscoelasticity coefficients are a generalization of the Leslie viscosity coefficients a_k through analytical continuation, and depend on the complex frequency s. The vector $\tilde{N}_i$ is defined as the sum of the substantial derivative of $\tilde{n}_i$ and the rotation of the fluid with respect to the director, and is more conveniently expressed in real space as

$$\vec{N} = \partial_t \vec{n} + (\vec{v} \cdot \nabla)\vec{n} - (\nabla \wedge \vec{v}) \wedge \vec{n} \Big/ 2.$$

The nematic field $\vec{n}$ is determined from the equilibrium of moments created by the viscoelastic stresses on the fluid and by the elastic stresses on the nematic, whose ratio is quantified by the Ericksen number, Er. In the limit of $Er \ll 1$, the viscoelastic forces on the fluid generated by the motion of the particle are small enough to not perturb the nematic field, and $\vec{n}$ will be equal to the equilibrium distribution[33]. In a typical PTM experiment the low Ericksen number hypothesis is reasonable far away from the particle. Thus, for the sake of studying the correlated motion of pairs of distant particles to formulate D2PTM, we assume the director field to be uniform in space and constant in time, $\vec{n} = (1, 0, 0)$.

To reduce the number of free material parameters, we group the viscoelasticity coefficients into three generalized Miesowicz[34] shear moduli,

$$\tilde{G}_a = \tilde{\alpha}_4^* \Big/ 2,$$
$$\tilde{G}_b = (\tilde{\alpha}_3^* + \tilde{\alpha}_4^* + \tilde{\alpha}_6^*) \Big/ 2,$$
$$\tilde{G}_c = (-\tilde{\alpha}_2^* + \tilde{\alpha}_4^* + \tilde{\alpha}_5^*) \Big/ 2,$$

and make use of Parodi's relation[35], $\tilde{\alpha}_6^* = \tilde{\alpha}_2^* + \tilde{\alpha}_3^* + \tilde{\alpha}_5^*$. Under these simplifications, equation (1) becomes

$$\partial_x \tilde{\bar{p}} = (\tilde{G}_c - \tilde{G}_a + \tilde{\alpha}_1^*) \partial_{xx} \tilde{u}_x + \tilde{G}_b \nabla^2 \tilde{u}_x + \tilde{f}_x, \quad (3)$$

$$\partial_y \tilde{\bar{p}} = \quad (\tilde{G}_c - \tilde{G}_a) \partial_{xx} \tilde{u}_y + \tilde{G}_a \nabla^2 \tilde{u}_y + \tilde{f}_y, \quad (4)$$

$$\partial_z \tilde{\bar{p}} = \quad (\tilde{G}_c - \tilde{G}_a) \partial_{xx} \tilde{u}_z + \tilde{G}_a \nabla^2 \tilde{u}_z + \tilde{f}_z, \quad (5)$$

where $\widetilde{\bar{p}} = \widetilde{p} + (\widetilde{G}_c - \widetilde{G}_a - \widetilde{\alpha}_5^*)\partial_x \widetilde{u}_x$ is a modified pressure, and $\overrightarrow{r} = (x, y, z)$ and $\overrightarrow{\widetilde{u}} = (\widetilde{u}_x, \widetilde{u}_y, \widetilde{u}_z)$ are the position and displacement vectors in a Cartesian coordinate system.

The three Miesowicz coefficients have a clear physical meaning in a nematic fluid[36]. For a uniform shear flow along the x-direction, $\widetilde{G}_b$ and $\widetilde{G}_c$ are excited if $\overrightarrow{n}$ is respectively parallel to the flow velocity or to the velocity gradient, whereas $\widetilde{G}_a$ is excited if $\overrightarrow{n}$ is perpendicular to both the flow velocity and its gradient. Fig. 14 in Appendix A provides a graphical interpretation of these coefficients.

2.2   Derivation of the Response Function

A spherical particle of radius a moving at low Reynolds number experiences a drag force that is proportional to its velocity,

$$\overrightarrow{\widetilde{F}} = -\overline{\overline{\widetilde{\zeta}}} \cdot \overrightarrow{\widetilde{v}}(\overrightarrow{x} = \overrightarrow{0}) = -\overline{\overline{\widetilde{\zeta}}} \cdot \overrightarrow{\widetilde{v}}_0 = -s\overline{\overline{\widetilde{\zeta}}} \cdot \overrightarrow{\widetilde{u}}_0, \quad (6)$$

where $\overline{\overline{\widetilde{\zeta}}}$ is the tensorial *Response Function*, also known as *Hydrodynamic Resistance*[37] or *Self-Resistance*[38]. Note that $\overrightarrow{\widetilde{v}}_0$ and $\overrightarrow{\widetilde{F}}$ are not parallel to each other in an anisotropic fluid as $\overline{\overline{\widetilde{\zeta}}}$ is not proportional to the identity matrix.

To calculate the response function of the particle, we perform a multipole expansion[37,39,40]. We first calculate the Green's function of equations (3)–(5) in the Fourier wavenumber domain, and then integrate the Green's function to obtain the particle velocity as a function of the driving force. Due to the linearity of the problem, we seek for solutions of the form

$$\overrightarrow{\widehat{v}} = \frac{\overline{\overline{\widehat{\mathscr{G}}}} \cdot \overrightarrow{\widehat{f}}}{8\pi} = \frac{1}{8\pi} \begin{Bmatrix} \widehat{\mathscr{G}}_{1j}\widehat{f}_j \\ \widehat{\mathscr{G}}_{2j}\widehat{f}_j \\ \widehat{\mathscr{G}}_{3j}\widehat{f}_j \end{Bmatrix}, \quad (7)$$

$$\widehat{\bar{p}} = \frac{\overrightarrow{\widehat{\mathscr{P}}} \cdot \overrightarrow{\widehat{f}}}{8\pi} = \frac{1}{8\pi}\widehat{\mathscr{P}}_j\widehat{f}_j, \quad (8)$$

where $\widehat{\cdot}$ denotes Fourier transform along the spatial coordinates, $\widehat{\mathscr{G}}_{ij}$ and $\widehat{\mathscr{P}}_j$ are the Green's functions for the velocity and the pressure, and $\overrightarrow{\widehat{f}}$ is the driving force applied on the fluid. Solving for the Green's functions of the problem yields (see[26] for more details)

$$\frac{\widehat{\mathscr{P}}_j}{\sqrt{8/\pi}} = \sqrt{-1}k_j\frac{(1-\delta_{1j})c + b}{d}, \quad (9)$$

and

$$\frac{\widehat{\mathscr{G}}_{1j}}{s\sqrt{8/\pi}} = \frac{\delta_{1j}k^2 - k_1k_j}{d}, \quad (10)$$

$$\frac{\widehat{\mathscr{G}}_{lj}}{s\sqrt{8/\pi}} = \frac{\delta_{lj}}{b} - k_lk_j\frac{(1-\delta_{1j})c + b}{db}, \quad (11)$$

with $l = 2,3$, and where

$$b(\vec{\mu};\vec{k}) = (\widetilde{G}_c - \widetilde{G}_a)k_1^2 + \widetilde{G}_ak^2,$$
$$c(\vec{\mu};\vec{k}) = \widetilde{\alpha}_1^* k_1^2 + (\widetilde{G}_b - \widetilde{G}_a)k^2,$$
$$d(\vec{\mu};\vec{k}) = \widetilde{\alpha}_1^* k_1^2(k_2^2 + k_3^2) + \widetilde{G}_b k^4 + (\widetilde{G}_c - \widetilde{G}_b)k_1^2 k^2,$$

$\vec{k} = (k_1, k_2, k_3) = (k_x, k_y, k_z)$ is the wavenumber vector, $\vec{\mu} = (\widetilde{\alpha}_1^*, \widetilde{G}_a, \widetilde{G}_b, \widetilde{G}_c)$ is the viscoelasticity vector, and δ_{ij} is the Kronecker delta.

The particle velocity is calculated by performing the inverse Fourier transform of equation (7) particularized at $\vec{x} = \vec{0}$,

$$\widetilde{\vec{v}}_0 = \frac{1}{(2\pi)^{3/2}} \int\int\int \frac{\widehat{\widetilde{\mathscr{G}}}}{8\pi} \cdot \widehat{\vec{f}}(\vec{k})d^3k = -\widetilde{\widetilde{\zeta}}^{-1} \cdot \widetilde{\vec{F}}, \quad (12)$$

where $\widehat{\vec{f}}(\vec{k}) = \vec{f} \cdot \widehat{H}(\vec{k})$ is the Fourier transfonn of $\vec{f}(\vec{x})$ and the function $\widehat{H}(\vec{k})$ is a regularization kernel that localizes the drag force in physical and/or Fourier space. We choose to distribute the force as a Gaussian around the origin[41,42] so that

$$\widehat{H}(k) = e^{-a^2k^2/\pi}. \quad (13)$$

The response function is thus given by

$$\tilde{\tilde{\zeta}}^{-1}\Big|_{ij} = \frac{s}{4\sqrt{2\pi}a} \int_{\theta=0}^{\theta=\pi} \sin\theta \left(\int_{\varphi=0}^{\varphi=2\pi} \frac{k^2 \widehat{\mathscr{G}}_{ij}}{8\pi} d\varphi \right) d\theta, \quad (14)$$

where $\vec{k} = (k, \phi, \theta)$ is the Fourier wavenumber vector in spherical coordinates. Due to the symmetry of $\widehat{\mathscr{G}}_{ij}$, the tensor $\tilde{\tilde{\zeta}}^{-1}$ is diagonal and equation (6) becomes

$$\vec{\widetilde{F}} = -s \begin{bmatrix} \tilde{\zeta}_\parallel & 0 & 0 \\ 0 & \tilde{\zeta}_\perp & 0 \\ 0 & 0 & \tilde{\zeta}_\perp \end{bmatrix} \cdot \vec{\widetilde{u}}_0, \quad (15)$$

where $\tilde{\zeta}_\parallel$ and $\tilde{\zeta}_\perp$ are respectively the components of the response function in the directions parallel and perpendicular to $\vec{n}$. Their general form is provided in Appendix A (equations 46 and 47) together with its singularities and Taylor expansion around the isotropy point.

The influence of the parameter $\tilde{\alpha}_1^*$ in the response function has been shown to be weak compared to that of the other coefficients[26], and its value has been measured to be very small for many nematic materials[43–47]. Thus, we focus on the limit case $\tilde{\alpha}_1^* \to 0$, for which the principal components of the response function are defined by

$$s\tilde{\zeta}_\parallel\Big|_{\tilde{\alpha}_1^* \to 0} = \frac{4\pi a(\tilde{G}_c - \tilde{G}_b)}{\dfrac{\tilde{G}_c}{\tilde{G}_b} \dfrac{\arctan\left(\sqrt{\tilde{G}_c/\tilde{G}_b - 1}\right)}{\sqrt{\tilde{G}_c/\tilde{G}_b - 1}} - 1}, \quad (16)$$

$$s\tilde{\zeta}_\perp\Big|_{\tilde{\alpha}_1^* \to 0} =$$

$$\frac{8\pi a(\tilde{G}_c - \tilde{G}_b)}{1 - \dfrac{\arctan\left(\sqrt{\tilde{G}_c/\tilde{G}_b - 1}\right)}{\sqrt{\tilde{G}_c/\tilde{G}_b - 1}} + \dfrac{\tilde{G}_c - \tilde{G}_b}{\tilde{G}_a} \dfrac{\arctan\left(\sqrt{\tilde{G}_c/\tilde{G}_a - 1}\right)}{\sqrt{\tilde{G}_c/\tilde{G}_a - 1}}}, \quad (17)$$

which exclusively depend on the three generalized Miesowicz shear moduli.

2.3   Particle-Particle Hydrodynamic Interactions in a Nematic Complex Fluid

Consider two distant particles denoted α and β, embedded in a nematic complex fluid as shown in Fig. 2, where a_α and a_β represent the particle radii, $\vec{r}_{\alpha,\beta}$ is the vector that connects the center of the particles, and $\left\|\vec{r}_{\alpha,\beta}\right\| \gg a_\alpha, a_\beta$.

When particle β moves with velocity $\widetilde{\vec{v}}^{\,0}_\beta$ it displaces the fluid around itself and induces a velocity

$$\widetilde{\vec{v}}^{\,I}_{\alpha,\beta} = \frac{\widetilde{\widetilde{\mathcal{G}}} \cdot \widetilde{\widetilde{\zeta}}}{8\pi} \cdot \widetilde{\vec{v}}^{\,0}_\beta \quad (18)$$

on particle α. Contrary to the isotropic case, the induced velocity depends not only on the distance between particles, $|\vec{r}_{\alpha,\beta}|$, but also on the orientation of $\vec{r}_{\alpha,\beta}$ with respect to the nematic director. Up to first order, the induced velocity will create an additional drag force on particle α,

$$\widetilde{\vec{F}}_\alpha = -\widetilde{\widetilde{\zeta}} \cdot \left(\widetilde{\vec{v}}^{\,0}_\alpha + \frac{\widetilde{\widetilde{\mathcal{G}}}}{8\pi} \cdot \widetilde{\widetilde{\zeta}} \cdot \widetilde{\vec{v}}^{\,0}_\beta \right). \quad (19)$$

Reciprocally, the total velocity of particle α is

$$\widetilde{\vec{v}}_\alpha = -\widetilde{\widetilde{\zeta}}^{\,-1} \cdot \widetilde{\vec{F}}^{\,0}_\alpha - \frac{\widetilde{\widetilde{\mathcal{G}}}}{8\pi} \cdot \widetilde{\vec{F}}^{\,0}_\beta. \quad (20)$$

The dependence between the velocities and drag forces of both particles can be expressed in matrix form[38] as

$$\begin{bmatrix} \widetilde{\vec{F}}_\alpha \\ \hline \widetilde{\vec{F}}_\beta \end{bmatrix} = -\widetilde{\widetilde{\mathscr{L}}} \cdot \begin{bmatrix} \widetilde{\vec{v}}_\alpha \\ \hline \widetilde{\vec{v}}_\beta \end{bmatrix}, \quad (21)$$

where $\widetilde{\widetilde{\mathscr{L}}}(\vec{r}\,; s)$ is the *multiparticle resistance tensor* and its inverse is the *multiparticle mobility tensor*. When the two particles are far apart from each other their long range interaction is very weak, and each particle's self-induced drag force dominates over their mutually-induced force. In that case, the resistance and mobility tensors up to first order become

$$\widetilde{\overline{\overline{\mathscr{L}}}} \approx \left[\begin{array}{c|c} \widetilde{\overline{\overline{\zeta}}} & \widetilde{\overline{\overline{\zeta}}} \cdot \widetilde{\overline{\overline{\mathscr{G}}}} \cdot \widetilde{\overline{\overline{\zeta}}} \Big/ 8\pi \\ \hline \widetilde{\overline{\overline{\zeta}}} \cdot \widetilde{\overline{\overline{\mathscr{G}}}} \cdot \widetilde{\overline{\overline{\zeta}}} \Big/ 8\pi & \widetilde{\overline{\overline{\zeta}}} \end{array} \right] \quad (22)$$

and

$$\widetilde{\overline{\overline{\mathscr{L}}}}^{-1} \approx \left[\begin{array}{c|c} \widetilde{\overline{\overline{\zeta}}}^{-1} & \widetilde{\overline{\overline{\mathscr{G}}}} \Big/ 8\pi \\ \hline \widetilde{\overline{\overline{\mathscr{G}}}} \Big/ 8\pi & \widetilde{\overline{\overline{\zeta}}}^{-1} \end{array} \right]. \quad (23)$$

This result is essential to derive D2PTM fonnulae in §2.5 below. To this end, it is necessary to transform the Fourier expressions (10)–(11) of the Green's function back into the physical domain. For a nematic fluid, it is sufficient to obtain the inverse transform particularized at $z = 0$ due to the axial symmetry of the nematic configuration. To exploit this symmetry, we work on the plane defined by $\vec{n}$ and $\vec{r}_{\alpha,\beta}$ and apply a simple rotation of the coordinate system to transform this plane into $z = 0$. The general form $\overline{\overline{\mathscr{G}}}(x, y, z = 0)$ is given in Appendix B (equations 58–63), along with its singularities and Taylor expansion around the isotropy condition. In the limit $\widetilde{\alpha}_1^* \to 0$, the components of the Green's function are

$$\frac{\widetilde{\mathscr{G}}_{11}}{s}\bigg|_{\substack{z=0 \\ \widetilde{\alpha}_1^* \to 0}} = \frac{2}{\widetilde{G}_b - \widetilde{G}_c} \left(\frac{1}{\sqrt{x^2 + y^2}} - \frac{\widetilde{G}_c}{\widetilde{G}_b} \frac{1}{\sqrt{x^2 + \frac{\widetilde{G}_c}{\widetilde{G}_b} y^2}} \right), \quad (24)$$

$$\frac{\widetilde{\mathscr{G}}_{12}}{s}\bigg|_{\substack{z=0 \\ \widetilde{\alpha}_1^* \to 0}} = \frac{2}{\widetilde{G}_b - \widetilde{G}_c} \frac{x}{y} \left(\frac{-1}{\sqrt{x^2 + y^2}} + \frac{1}{\sqrt{x^2 + \frac{\widetilde{G}_c}{\widetilde{G}_b} y^2}} \right), \quad (25)$$

$$\frac{\widetilde{\mathscr{G}}_{22}}{s}\bigg|_{\substack{z=0 \\ \widetilde{\alpha}_1^* \to 0}} = \frac{2}{\widetilde{G}_b - \widetilde{G}_c} \frac{x^2}{y^2} \left[\frac{1}{\sqrt{x^2 + y^2}} - \frac{\widetilde{G}_b}{\widetilde{G}_c} \frac{1}{\sqrt{x^2 + \frac{\widetilde{G}_c}{\widetilde{G}_b} y^2}} \right.$$
$$\left. + \frac{1}{x^2} \left(\frac{\widetilde{G}_b}{\widetilde{G}_c} - 1 \right) \sqrt{x^2 + \frac{\widetilde{G}_c}{\widetilde{G}_a} y^2} \right], \quad (26)$$

$$\left.\frac{\widetilde{\mathscr{G}}_{33}}{s}\right|_{\substack{z=0 \\ \widetilde{\alpha}_1^* \to 0}} = \frac{2}{\widetilde{G}_b - \widetilde{G}_c}\frac{1}{y^2}\left[-\sqrt{x^2+y^2}+\frac{\widetilde{G}_b}{\widetilde{G}_c}\sqrt{x^2+\frac{\widetilde{G}_c}{\widetilde{G}_b}y^2}\right.$$

$$\left.-\left(\frac{\widetilde{G}_b}{\widetilde{G}_c}-1\right)\frac{x^2}{\sqrt{x^2+\frac{\widetilde{G}_c}{\widetilde{G}_a}y^2}}\right]. \tag{27}$$

2.4 Directional One-Point Particle Tracking Microrheology: An Undetermined Problem

The Einstein relation between the one-dimensional mean squared displacements (MSD) of a particle undergoing Brownian motion and its hydrodynamic drag is

$$\widetilde{\zeta} = \frac{2k_BT}{s^2\langle\Delta x(0), \Delta\widetilde{x}(s)\rangle}, \tag{28}$$

where k_B is the Boltzmann constant, T the temperature and $\langle\Delta x(0), \Delta\widetilde{x}(s)\rangle$ the Laplace transform of the MSD[4,48]. Using the results derived in §2.1–2.2, this Einstein equation can be adapted to describe the motion of a particle embedded in a nematic complex fluid.

In the principal directions defined by $\overrightarrow{n}$ and its orthogonal plane, the response function tensor is diagonal (see equation 15). Thus, the MSD measured in these principal directions are independent of each other (zero cross-correlation) and equation (28) can be applied separately along each principal direction[12,20,21], yielding

$$6\pi a\widetilde{G}_{\text{eff, }\parallel} = s\widetilde{\zeta}_\parallel = \frac{2k_BT}{s\langle\Delta x_\parallel(0), \Delta\widetilde{x}_\parallel(s)\rangle}, \tag{29}$$

$$6\pi a\widetilde{G}_{\text{eff, }\perp} = s\widetilde{\zeta}_\perp = \frac{2k_BT}{s\langle\Delta x_\perp(0), \Delta\widetilde{x}_\perp(s)\rangle}. \tag{30}$$

However, it is important to note that these two equations together with (16)–(17), are not sufficient to determine the three Miesowicz shear moduli $\widetilde{G}_a$, $\widetilde{G}_b$ and $\widetilde{G}_c$[26]. The next section shows that analyzing the correlated motion of pairs of distant particles resolves this indetermination.

2.5 Directional Two-Point Particle Tracking Microrheology

Consider two distant particles whose coordinates and velocity components are represented by $x_{a,i}$ and $v_{a,i}$ in a Cartesian coordinate system with its $x_1 = x_\parallel$ direction parallel to $\vec{n}$, its $x_2 = x_\perp$ direction contained in the plane defined by the two particles and $\vec{n}$, and the $x_3 = z$ direction perpendicular to said plane (see Fig. 2). The two particles are thus contained in the plane $z = 0$ and equations (24)–(27) hold. Following Squires and Mason[38], we obtain that

$$\left\langle \Delta x_{\alpha,i}(0), \Delta \widetilde{x}_{\beta,j}(s) \right\rangle = \frac{2k_B T}{s^2} \left[\widetilde{\mathscr{L}}^{-1}(\vec{r}_{\alpha,\beta}; s) \right]_{i,j}, \quad (31)$$

where $\widetilde{\overline{\overline{\mathscr{L}}}}(\vec{r}; s)$ is the multiparticle resistance tensor derived in §2.3, whose inverse is given in equation (23). The upper left and lower right blocks of (23) provide the one-point directional PTM formula derived by Gómez-González and del Álamo[26] (summarized in §2.4). The off-diagonal blocks of the tensor provide the two-point formulae

$$\left\langle \Delta x_{\alpha,i}(0), \Delta \widetilde{x}_{\beta,j}(s) \right\rangle = \frac{k_B T}{4\pi s^2} \widetilde{\mathscr{G}}_{ij}, \quad \alpha \neq \beta. \quad (32)$$

This symmetric tensor relation offers six equations for $\widetilde{G}_a$, $\widetilde{G}_b$ and $\widetilde{G}_c$ but these equations are not linearly independent. The tensorial incompressibility condition $\nabla \cdot \overline{\overline{\mathscr{G}}} = \vec{0}$ establishes three constraints on the elements of $\widetilde{\mathscr{G}}_{ij}$, effectively reducing the number of independent equations in (32) to three.

In the ideal experimental scenario where one could measure 3D particle displacements as a function of time, it would be convenient to use the diagonal equations of (32) to calculate the Miesowicz shear moduli from the measured two-point mobility tensor. However, typical experiments only provide accurate measurements of 2D particle displacements. In this scenario, it is still possible to calculate the three Miesowicz shear moduli from the equations corresponding to $\widetilde{\mathscr{G}}_{11}$, $\widetilde{\mathscr{G}}_{12}$ and $\widetilde{\mathscr{G}}_{22}$, but it is advisable to precondition the equations as described below to minimize numerical error.

The cross-correlated displacements in the left hand side of (32) have very low values due to the low energy and long range of the particle-particle interactions. Thus, it is necessary to compile averages over a large number of particle pairs to obtain statistically meaningful results. But since $\widetilde{\mathscr{G}}_{ij} \sim r_{\alpha,\beta}^{-1}$, the averaging procedure converges faster if equation (32) is renormalized by $r_{a,\beta}$. Additionally, $\widetilde{\mathscr{G}}_{12}$ is typically much smaller than $\widetilde{\mathscr{G}}_{11}$ and $\widetilde{\mathscr{G}}_{22}$, which can lead to numerical errors when jointly solving the three equations. Considering that $\widetilde{\mathscr{G}}_{12} \sim x \left/ (y\sqrt{x^2 + y^2})\right.$, we use this factor to renormalize the corresponding equation. The resulting system of equations for the calculation of the Miesowicz shear moduli is

$$\sum_{\alpha,\beta} r_{\alpha,\beta} \left\langle \Delta x_{\alpha,\,\parallel}(0), \Delta \widetilde{x}_{\beta,\,\parallel}(s) \right\rangle = \frac{k_B T}{4\pi s^2} \cdot \sum_{\alpha,\beta} r_{\alpha,\beta} \widetilde{\mathcal{G}}_{11}(\overrightarrow{r};s), \quad (33)$$

$$\sum_{\alpha,\beta} \frac{y}{x} r_{\alpha,\beta} \left\langle \Delta x_{\alpha,\,\parallel}(0), \Delta \widetilde{x}_{\beta,\,\perp}(s) \right\rangle = \frac{k_B T}{4\pi s^2} \cdot \sum_{\alpha,\beta} \frac{y}{x} r_{\alpha,\beta} \widetilde{\mathcal{G}}_{12}(\overrightarrow{r};s), \quad (34)$$

$$\sum_{\alpha,\beta} r_{\alpha,\beta} \left\langle \Delta x_{\alpha,\,\perp}(0), \Delta \widetilde{x}_{\beta,\,\perp}(s) \right\rangle = \frac{k_B T}{4\pi s^2} \cdot \sum_{\alpha,\beta} r_{\alpha,\beta} \widetilde{\mathcal{G}}_{22}(\overrightarrow{r};s), \quad (35)$$

where α and β represent every possible particle pair in the experimental domain. Equations (33)–(35) form a non-linear system that must be solved iteratively for each Laplace frequency. In this system, k_B is a physical constant, s is a parameter of the problem, while T, $\overrightarrow{r}_{\alpha,\beta}$ and $\Delta x_{i,j}$ are experimental measurements, and $\widetilde{\mathcal{G}}_{i,j}$ are provided by equations (24)–(27). Once the experimental measurements are defined, the only three unknowns of the problem are $\widetilde{\mathcal{G}}_a$, $\widetilde{\mathcal{G}}_b$ and $\widetilde{\mathcal{G}}_c$.

Fig. 3 presents a flow chart summarizing the D2PTM analysis. We first track the embedded probing particles in two orthogonal directions x and y that define a plane containing the director of the fluid, $\overrightarrow{n}$. We then calculate the ensemble averaged MSD, *i.e.* $\left\langle \Delta x^2(\tau) \right\rangle$, $\left\langle \Delta y^2(\tau) \right\rangle$ and $\left\langle \Delta x, \Delta y(\tau) \right\rangle$. From these data, we calculate their principal directions $x_\parallel$ and $x_\perp$, *i.e.* the two orthogonal directions where the cross-MSD term $\left\langle \Delta x_\parallel, \Delta x_\perp(\tau) \right\rangle$ is zero (down to experimental error). Then, we calculate the two-point MSD of each particle pair in principal directions and solve equations (33)–(35) to obtain the values of $\widetilde{\mathcal{G}}_a(s)$, $\widetilde{\mathcal{G}}_b(s)$ and $\widetilde{\mathcal{G}}_c(s)$.

3 Materials and Methods

3.1 Experimental Methods

3.1.1 Sample preparation

3.1.1.1 Nematic F-actin solutions: F-actin samples were prepared following well-established protocols[21,49]. Preformed actin filaments from rabbit skeletal muscle were purchased from Cytoskeleton, Inc. (Denver, CO). This F-actin mixture was diluted in Milli-Q water at room temperature to a concentration of 0.4 mg/ml. The resulting F-actin solution contained 5 mM Tris HC1 pH 8.0, 0.2 mM $CaCl_2$, 0.2 mM ATP, 2 mM $MgCl_2$ and 5% (w/v) sucrose. The samples were incubated for 10 minutes at room temperature, allowing the filaments to completely dissociate from each other. In order to protect the samples from bacterial growth, ampicillin was added to a final concentration of 100 µg/ml. The salt concentration of the buffer produces an average filament length of 8 µm, which is substantially smaller than the persistence length of F-actin, $\xi_p \sim 20$ µm[50]. Thus, the actin

filaments in our experiments can be safely assumed to be straight. To induce the nematic transition of the samples, the F-actin concentration was increased to 4 mg/ml while keeping constant the salt concentration and filament length by dialyzing the sample, *i.e.* the sample was centrifuged at 2,000 g and 19°C in an Amicon Ultra-4 Centrifugal Filter Unit (EMD Millipore, Billerica, MA) until the target concentration was reached. The protein concentration was monitored using a spectrophotometer to measure the absorbance at 650 nm.

Carboxylate modified red latex beads with 0.5 µm nominal diameter (Fluospheres, Invitrogen, Carlsbad CA) were diluted in the supernatant solution and then added to the protein solution. The surface chemistry of the probing particles is not determinant for the experiments, given that the near-field effects are negligible for the two-point particle tracking microrheology experiments. Likewise, the particle size is also not important, as long as the interparticle separation is much larger than the particle radii[17]. The protein solution with beads was stored at 4°C for no longer than a week. Rectangular capillary tubes with internal dimensions 0.1 mm × 1 mm × 50 mm (VitroCom, Mountain Lakes, NJ) were filled through capillarity with the protein solution. The filling flow provides enough shear to align the F-actin filaments parallel to the capillary axis (Fig. 11*a* and ref.[21]). The tubes were sealed with two-component epoxy resin to avoid evaporation and internal currents, and attached to a microscope glass slide. The samples were kept at room temperature for at least 2 hours to reach thermal equilibrium in preparation for imaging.

3.1.1.2   Disodium cromoglycate nematic liquid crystal: Following the protocol outlined in[51,52], 14%wt and 16%wt samples of DSCG in water were prepared. They were mixed for 12 hours to ensure proper dissolution. Prior to the experiments, they were heated for about 15 minutes to 65°C, above their isotropic to nematic transition, to ensure that any residual nematic alignment was eliminated. After cooling the samples to the experimental temperature, *i.e.* 21°C, 0.2 μm diameter fluorescent spheres were injected and the samples were inserted in the imaging chambers, as described in §3.1.1.1.

3.1.2   Microscopy and Image Processing—Fluorescent light image sequences of the samples were captured at 50 Hz, during 100-300 seconds, using a Feica DMI6000 B inverted microscope (Leica Microsystems, Inc., Buffalo Grove, IL), equipped with a Zyla 4.2 sCMOS camera (Andor Technology Ftd., Belfast, UK) and a 63X oil immersion objective lens, and mounted on a Micro-g 63-543 optical air table (TMC - AMETEK, Inc.) that damped vibrations. The imaging setup was controlled by the open source microscopy software Micro-Manager [53–55].

The centers of the fluorescent particles were tracked by implementing a previously reported algorithm[56] that we validated for Newtonian fluids (see Appendix E). From the trajectories of the particles, we calculated the one-point MSD in the directions parallel and perpendicular to $\overrightarrow{n}$, and the two-point cross-MSD for pairs of distant particles. Fig. 4 shows particle trajectories obtained in a typical experiment. We then analyzed the cross-MSD as described in §2.5 to determine the directional shear moduli of the F-actin solution (see Fig. 3). A total of 20 F-actin samples were analyzed. For each sample, images from different

regions were taken, capturing the motion of 2 to 10 particles in each image, for a total of 2,346 particles and 6,105 particle pairs.

3.2 Numerical Methods

3.2.1 Brownian Motion Simulations

3.2.1 Brownian Motion Simulations—For validation purposes, we performed numerical simulations of particle Brownian motion in viscoelastic nematic fluids. In these simulations, we prescribed the Miesowicz shear moduli using a Kelvin-Voigt model $\widetilde{G}_k = \mu_k + s \cdot \eta_k$ with constant μ_k and η_k. The Brownian motion experienced by each particle was defined as a Gaussian process with average and autocorrelation consistent with the fluctuation-dissipation theorem[57,58]:

$$\left\langle v_x(t) \right\rangle = \left\langle v_y(t) \right\rangle = \left\langle v_z(t) \right\rangle = 0, \quad (36)$$

$$\left\langle v_x(t), v_x(t+\tau) \right\rangle = \mathscr{L}^{-1}\left(\frac{2k_B T}{ms + \widetilde{\zeta}_\parallel(s)}; s \to \tau \right), \quad (37)$$

$$\left\langle v_y(t), v_y(t+\tau) \right\rangle = \left\langle v_z(t), v_z(t+\tau) \right\rangle = $$
$$= \mathscr{L}^{-1}\left(\frac{2k_B T}{ms + \widetilde{\zeta}_\perp(s)}; s \to \tau \right), \quad (38)$$

where $\mathscr{L}^{-1}(\cdot \, ; s \to t)$ represents the inverse Laplace transform. Since the particles are small, we assumed that inertial forces were negligible compared with the hydrodynamic forces acting on them, i.e. $ms \ll \widetilde{\zeta}_j(s)$. This assumption has been shown to be valid for the frequencies accessible to PTM experiments [15,26].

By virtue of the central limit theorem, it can be shown that equations (36), (37) and (38) describe three multivariate normal distributions, one for the velocity in each direction[59]. Each distribution was completely defined by a zero average vector and a covariance matrix $\overline{\overline{\Sigma}}_\parallel$ or $\overline{\overline{\Sigma}}_\perp$ with components

$$\Sigma_{\parallel,kl} = 2k_B T \cdot \mathscr{L}^{-1}\left(\widetilde{\zeta}_\parallel^{-1}(s); s \to \tau \right)\Big|_{\tau = t_k - t_l}, \quad (39)$$

$$\Sigma_{\perp,kl} = 2k_B T \cdot \mathscr{L}^{-1}\left(\widetilde{\zeta}_\perp^{-1}(s); s \to \tau \right)\Big|_{\tau = t_k - t_l}. \quad (40)$$

We prescribed fixed values for μ_a, μ_b, μ_c, and η_a η_b, η_c, and calculated the covariance matrices (39) and (40). The time distribution of velocities for each particle, $\vec{v}_\alpha^0(t)$, is drawn from a Multivariate Random Number generator. Fig. 5 shows the parallel and perpendicular covariance kernels calculated from (39)–(40) for $\mu_a = 0.5$ Pa, $\mu_b = 0.01$ Pa, $\mu_c = 1$ Pa and $\eta_a = \eta_b = \eta_c = 0.1$ Pa·s, compared to the ensemble-averaged autocorrelation of the random velocity samples for 10,000 time steps and 3,325 particles. The plot shows that the autocorrelation closely follows the prescribed covariance kernels, indicating that the simulation procedures are self-consistent.

In each simulation we considered five particles initially located at a distance higher than ten radii from each other. This configuration is representative of the experiments presented in §5. From the simulated Brownian motion of the particles, we calculated the hydrodynamic interactions between pairs of particles as described in §2.3. The computation of these interactions was accelerated by exploiting the fact that the jumps in particle position are negligible compared to the inter-particle distance, which allowed us to assume constant $\vec{r}(s)$. Thus, for each pair of particles, it was necessary to evaluate the Green's functions only once (24)–(26) to calculate the induced velocity from (18).

After the hydrodynamic interactions are calculated, the velocity of each particle is obtained as the sum of its own Brownian motion and the particle-particle interaction terms,

$$\widetilde{\vec{v}}_\alpha = \widetilde{\vec{v}}_\alpha^0 + \sum_{\forall \beta \neq \alpha} \widetilde{\vec{v}}_{\alpha,\beta}^I. \quad (41)$$

The final step of the simulation is to calculate the particle trajectories by integrating in time their velocity vector.

All the analysis and simulation tools were written in the general-purpose programming language Python[60] using the numerical and scientific packages Numpy[61] and Scipy[62], and the plotting library Matplotlib[63]. The most computationally intensive functions were compiled in C by using Cython[64], and sped up by using Memoryview objects and the linear algebra module Ceygen[65]. A key step of the simulations is to calculate direct and inverse Laplace transforms. The numerical implementation of these transforms is explained in §3.2.2 below.

Fig. 6(*a*) shows the random evolution of the velocity of a representative particle in the ∥ and ⊥ directions. The blue and red lines represent respectively the total velocity of the particle and the velocity induced by its four neighboring particles. The particle-particle interaction is a weak higher-order effect, and the total influence of the four neighbouring particles is smaller than the Brownian particle velocity. Fig. 6(*b*) shows the trajectories of the five particles in the same simulation. As noted above the inter-particle distance is much greater than the particle displacement, which justifies our assumption of constant particle-particle separation in the calculation of the Green's functions (24)–(26). The inset of Fig. 6(*b*) zooms into the trajectory of one particle, whose envelope is an ellipse with its major axis aligned

along the nematic, consistent with the anisotropic rheological properties of the simulated fluid.

3.2.2 Numerical implementation of Laplace transforms—Laplace transforms were calculated using the Fast Laplace Transform (FLT) approach[66]. The FLT is based on the observation that the complex Laplace frequency s is related to the Fourier frequency ω as $s = c + i\omega$, so that the Laplace transform can be calculated by using the coefficients of the Fast Fourier Transform. We used an efficient implementation of the Fast Fourier Transform called the FFTW[67,68]. The accuracy of the FLT was characterized as a function of the free frequency parameter c[66], being $c = 4\pi/T$ the optimal value, which we employed throughout the simulations. We found the errors introduced by the FLT for the specific data of our simulations to be $\sim 10^{-6}\%$[69]. We dismissed the implementation of an improved Talbot approximation to the Inverse Laplace Transform[70–72] because, while it would provide a smoother result, it is singular at $\tau = 0$.

4 Validation of D2PTM

In order to assess the feasibility and accuracy of D2PTM, we applied this new technique to measure the directional viscosities of a lyotropic chromonic nematic liquid crystal[73], and compared the results with reference values available in the literature[52]. Existing methods to measure the anisotropic rheology of liquid crystals typically assume constant viscosity coefficients. However, other complex fluids may exhibit nontrivial frequency dependence in their shear moduli, with both elastic and viscous components. In order to assess the capacity of D2PTM to capture these effects in nematic fluids, we also tested this technique in numerically simulated directional viscoelastic gels.

4.1 D2PTM of a lyotropic nematic liquid crystal

Water based liquid crystals such as disodium cromoglycate (DSCG)[52,73] are a convenient benchmark for D2PTM since the probing microparticles are easily available as a water suspension. DSCG is a lyotropic chromonic nematic liquid crystal that has recently sparked attention due to its biocompatibility[51] and other interesting properties[74]. We chose DSCG because its directional viscosity coefficients were previously characterized by means other than D2PTM. Zhou *et al.*[52] measured the twist viscosity (η_{twist}) of DSCG, as well as its splay (η_{splay}) and bend (η_{bend}) viscosities. These coefficients can be used to calculate two of the Miesowicz viscosities measured by D2PTM, namely η_b, and η_c [33], by solving the equations:

$$\eta_{splay} = \eta_{twist} - \alpha_3^2 \big/ \eta_b, \quad (42)$$

$$\eta_{twist} = \alpha_3 - \alpha_2, \quad (43)$$

$$\eta_{bend} = \eta_{twist} - \alpha_2^2 \Big/ \eta_c, \quad (44)$$

$$\eta_b - \eta_c = \alpha_2 + \alpha_3. \quad (45)$$

Table 1 displays the values of η_b and η_c calculated from by Zhou *et al.* 's measurements for two DSCG concentrations (14 wt% and 16 wt%). We prepared DSCG samples at these two concentrations as detailed in §3.1.1.2, and particle motion was imaged as explained in §3.1.2. Then, the motions of the probing particles were analyzed following our new D2PTM protocol, which is described in §2.5.

Fig. 7(*a*) shows the principal MSDs measured for probing microparticles immersed in a nematic 16 wt% DSCG solution. Due to the dominantly viscous nature of this fluid, the MSDs vary ahnost linearly with τ and the curves have a roughly unit slope for $\tau < 1000 s$. However, the slopes are not exactly one, and they are different along different directions, suggesting that the DSCG is, as expected, not completely viscous. Anyhow, given that there is not data available in the literature to compare with the measurement of the elastic response of the DSCG solutions, we will only regard the viscous part of its directional shear moduli. At longer time scales, the MSDs manifested a departure from linear slope, probably due to incomplete statistical convergence. Consistent with this explanation, the standard deviation of the MSDs increased significantly for $\tau > 100 s$, and we observed a similar long-time behavior for additional validation experiments performed in a Newtownian isotropic fluid (see Fig. 17 in Appendix E).

Fig. 7(*b*) displays the two-particle MSDs. The dependence of these data on τ is similar to that of their one-point counterparts and, as we had anticipated, the noise content of the cross-directional MSD (*i.e.* ∥–⊥) is higher. Also as expected, the renormalization proposed in (33)–(35) makes the values of the different two-point and one-point MSD components comparable to each other. We also measured one- and two-point MSDs of particles immersed in 14% wt DSCG (see Fig. 15 in Appendix D.1), and obtained qualitatively similar results. The Miesowicz viscosity coefficients obtained by D2PTM from our two-particle cross-MSD measurements are shown in Table 1. The results are in good agrent with those obtained from Zhou *et al.* 's [52] data for both the two DSCG concentrations that we considered in our experiments (14% and 16%). As a reference, we also include the directional effective friction coefficients that are obtained by analyzing the motion of single particles embedded in DSCG.

4.2 Validation of D2PTM by Numerical Simulation

To provide further validation of D2PTM, we simulated the Brownian motion of particles embedded in a nematic viscoelastic fluid of known Miesowicz viscoelasticity coefficients, including the particle-particle hydrodynamic interaction. The simulation procedures are detailed in §3.2.1 above. We then analyzed the simulated particle trajectories as described in

§2.5, and compared the shear moduli values obtained from this analysis with those initially prescribed in the Brownian motion simulation.

To determine the mean square displacement tensor, we simulated the trajectories of 200 particle groups each containing 5 particles (*i.e.* 2,000 particle pairs). For consistency, we considered the same nematic Kelvin-Voigt fluid with $\mu_a = 0.5$ Pa, $\mu_b = 0.01$ Pa, $\mu_c = 1$ Pa and $\eta_a = \eta_b = \eta_c = 0.1$ Pa·s used to illustrate the simulation methodology in Figs. 5 and 6. The directional one-point MSD of the simulated particles are plotted in Fig. 8(*a*) in principal directions of the fluid. Due to the particular choice of parameters for the Kelvin-Voigt model, these MSD have a characteristic shape. At low values of τ, the MSD are dominated by the high-frequency viscous response of the fluid and thus increase linearly with τ. Furthermore, since we prescribed the same value for η_a, η_b, and η_c, at short τ the MSD are isotropic (*i.e.* $\langle \Delta x_\parallel^2 \rangle = \langle \Delta x_\perp^2 \rangle$). In contrast with this behavior, the MSD are dominated by the low-frequency elastic response of the fluid at high values of τ, thereby reaching a plateau. Additionally, since we prescribed different values for μ_a, μ_b and μ_c, the MSD are different along different directions. Of note, the simulated MSD ratio $\langle \Delta x_\parallel^2 \rangle / \langle \Delta x_\perp^2 \rangle$ is non-trivially related to the ratios between the three shear moduli, consistent with the idea that the effective shear moduli obtained from eqs. (29)–(30) do not reflect the material viscosities of a nematic complex fluid[4,26].

Fig. 8(*b*) displays the two-point MSD of the simulated 2,000 particle pairs. Using these data as inputs, we solved equations (33)–(35) to determine the three Miesowicz complex shear moduli. Fig. 9 shows the loss (panel *a*) and storage (panel *b*) components of the complex moduli recovered from the simulated trajectories, together with the functional forms of these parameters initially prescribed in our simulations. The agreement between recovered and prescribed moduli is excellent for the whole range of frequencies considered. A similarly good agreement between prescribed and recovered shear moduli is found for different combinations of viscoelastic parameters (see Appendix D.2 for an additional example).

Together with the liquid crystal experiments presented above, these simulations suggest that D2PTM can be used to accurately determine the rheological properties of nematic complex fluids from measurements of particle trajectories.

5 Experimental Application of D2PTM to nematic F-actin solutions

This section illustrates the experimental application of D2PTM to characterize the rheological properties of a nematic complex fluid formed by a solution of filamentous actin (F-actin). Actin is the most abundant cytoskeletal protein in eukaryotic cells, and forms elongated fibers that can display nematic ordering and anisotropic rheology[12,21].

The qualitative anisotropic rheology of nematic F-actin solutions can be observed by plotting the histograms of the tracked particle jumps in the directions parallel and perpendicular to $\overrightarrow{n}$, $P[\Delta x_\parallel(\Delta t)]$ and $P[\Delta x_\perp (\Delta t)]$ (see ref.[21] and Fig. 10). Both histograms have similar skewness (S) and kurtosis (K) coefficients, namely $S_\parallel = -2.4 \times 10^{-3}$, $K_\parallel = 3.25$, and $S_\perp = 9 \times 10^{-4}$, $K_\perp = 3.22$. These values are also approximately consistent with a Normal distribution ($S = 0$, $K = 3$). The widths of these histograms are however markedly

different, indicating that particle mobility is anisotropic. The nematic director of the F-actin solution has been shown to align with the direction of highest mobility of the probing particles [21]. Thus, we define the ∥ direction as the principal direction of maximal mobility in our experiments, and the ⊥ direction as the orthogonal direction corresponding to minimal mobility. This assignment is confirmed by Fig. 11(a), which shows one-point MSD of the tracked particles along the axis of the capillary tube (x direction), the orthogonal direction (y), and the principal ∥ and ⊥ directions determined by diagonalizing the MSD tensor. The data shows that the MSD in the x and y directions respectively agree with the MSD in the ∥ and ⊥ directions, implying that the actin fibers were successfully aligned parallel to the capillary axis during sample preparation.

As expected, the MSD curves in Fig. 11(a) have slopes between 0 and 1, suggesting that the rheology of the F-actin solutions was neither purely elastic nor purely viscous in the range of time scales considered. The MSD ratio $\left\langle \Delta x_\parallel^2 \right\rangle / \left\langle \Delta x_\perp^2 \right\rangle$, shown in the inset of Fig. 11(a), ranges between 2 at low values of τ and 4 at high τ values, confirming the anisotropic behavior observed in the histograms of Fig. 10. Overall, these one-point MSD are in fair agreement with previously reported data[21].

The two-point directional MSD of the 6,105 tracked particle pairs are plotted in Fig. 11(b), expressed in principal directions and normalized as indicated in (33)–(35). The D2PTM analysis of the two-point MSD allowed us to calculate the complex shear moduli of the nematic F-actin solutions from our experimental measurements. These shear moduli are plotted in Fig. 12 as a function of frequency. As stated above, the inter-particle interactions are much weaker than the single particle thermal fluctuations, particularly the cross-direction component $\left\langle \Delta x_{\parallel,a}, \Delta x_{\perp,\beta} \right\rangle$ (see Fig. 11 b). As such, they are more prone to experimental noise, and a larger number of observations are needed in order to attain statistical convergence. Hence, in the results shown in Fig. 12 we have kept only the two highest frequency decades. Since Brownian motion is ergodic, the number of independent experimental observations increases linearly with ω, and statistical convergence improves for higher frequencies.

For the range of frequencies considered, the smallest moduli are G_c' and G_c''. We also observe that $G_a' > G_b'$ for all frequencies. On the other hand, $G_b'' > G_a''$ for high frequencies while the opposite happens for low frequencies. Notably, the loss moduli G_b'' and G_c'' monotonically increase with the frequency, with a slope that denotes a viscous-like behaviour. On the other hand, G_a'' varies more slowly with frequency, implying a more intricate viscoelastic behaviour.

To facilitate the interpretation of these results. Fig. 13 replots the Miesowicz moduli as $G_\parallel = G_b$, $G_\perp = G_a$ and $G_\Delta = G_c — G_a$, based on the form of the equations of motion (3)–(5). In this representation, $G_\parallel$ and $G_\perp$ reflect the anisotropy in the strain-stress relationship, while G_Δ indicates the bending resistance with respect to $\overrightarrow{n}$[26]. The data suggest that fluctuations perpendicular to the nematic likely generate distortions of the F-actin fibers including fiber bending, which trigger an elastic-like response, $i.e.$ the storage components of $G_\perp$ and G_Δ

are dominant. Conversely, fluctuations parallel to the nematic generate a viscous response dominated by $G''_\parallel$, and likely caused by filament-solvent sliding.

The anisotropic rheology of a nematic complex fluid can be fully characterized by one-point microrheology only in two particular pseudo-isotropic cases [26] in which the number of independent Miesowicz shear moduli is reduced to two. These cases are $G_a = G_b$, which corresponds with isotropic momentum diffusivity ($G_\parallel = G_\perp$), and $G_a = G_c$, which corresponds with zero resistance to bending ($G_\Delta = 0$). Our experimental results indicate that neither of these conditions are satisfied for nematic F-actin solutions. Fig. 13 compares the shear moduli obtained by D2PTM with the effective moduli obtained by one-point directional PTM, $G_{\text{eff},\parallel}$ and $G_{\text{eff},\perp}$ (equations 29–30 and refs.[12,20,21]). Apart from the obvious differences in magnitude, there is a number of notable qualitative differences between the effective one-point moduli and actual two-point ones. We observe that $|G_\Delta| \sim |G_\perp|$ suggesting that the response to nematic bending, which cannot be captured by one-point PTM, makes an important contribution to the microrheology of nematic F-actin solutions. More importantly, the one-point data would suggest that $G''_{\text{eff}, \parallel} < G''_{\text{eff}, \perp}$ despite that $G''_\parallel > G''_\perp$ (Fig. 13*a*), implying that one-point PTM may fail to identify the direction of maximum viscosity in nematic complex fluids. Additionally, one-point PTM underestimates $G'_\perp$ while it overestimates $G'_\parallel$ (Fig. 13*b*), thus severely underpredicting the level of anisotropy in the elastic response of nematic F-actin solutions.

6   Discussion and Conclusion

Soft viscoelastic materials often exhibit microstructural alignment along a common direction leading to anisotropic rheological properties. Liquid crystals[75], nematic viscoelastomers[76], the cell cytoplasm[12,77], and the extracellular matrix[78] are examples of nematic soft materials. For small distortions of the nematic direction field (*i.e.* low Ericksen number limit), the anisotropic rheology of nematic complex fluids can be approximately described by three frequency-dependent Miesowicz complex shear moduli[26,79,80]. These coefficients can be macroscopically measured by subjecting the sample to simple shear in different geometrical configurations[81,82], by propagating ultrasound waves or electromagnetic fields, and by light scattering techniques[83]. However, there is a lack of microscopic methods to characterize the rheological properties of nematic complex fluids. This paper introduces a novel particle tracking microrheology method to address this limitation: directional two-point particle tracking microrheology (D2PTM). Compared to existing macroscopic methods, D2PTM can be applied to minute samples and involves a simple experimental setup.

The theoretical foundation of D2PTM is established by extending previous analyses of nematic flow around a microrheological probe[26]. We determine the mutual hydrodynamic interactions between pairs of distant particles immersed in a nematic complex fluid, and we use this knowledge to generalize two-point particle-tracking microrheology[17] to these soft materials. This new analysis allows for calculating the three Miesowicz shear moduli from the measured cross-MSD of particle pairs. Further work would be needed to extend this derivation to smectic or cholesteric phases.

In order to experimentally validate D2PTM, we applied this new technique to disodium cromoglycate (DSCG), a lyotropic nematic liquid crystal whose directional viscosity coefficients were recently measured by dynamic light scattering methods[52]. These validation experiments suggest that D2PTM measurements agree well with measurements from previous methods. D2PTM was validated further by simulating the Brownian motion of spheres embedded in a nematic complex fluid with prescribed frequency-dependent Miesowicz shear moduli. We then applied the D2PTM analysis to the trajectories of the particles and recover the Miesowicz moduli, which resulted to be in close agreement with the prescribed ones.

To demonstrate the experimental application of D2PTM to nematic complex fluids with viscoelastic anisotropic rheology, we perform particle-tracking experiments on F-actin solutions where the actin filaments are aligned by flow shear. The one-point statistics of particle motion obtained in our experiments are consistent with those previously reported for similar F-actin solutions[21]. Moreover, D2PTM provides direct information about the microstructure of the material that is not accessible from one-point measurements of particle mobility. Specifically, we observed that the microrheological response of F-actin solutions is predominantly viscous in the direction parallel to $\overrightarrow{n}$ probably due to filament-solvent sliding, while their response is predominantly elastic in the perpendicular direction due to fiber distortions and fiber bending. This two-point analysis of particle trajectories revealed important differences between the true material shear moduli of nematic F-actin solutions, and the so-called effective shear moduli derived by previous one-point analyses[12,20,21]. In addition to not being able to capture the rotational shear modulus of the nematic, one-point PTM may incorrectly determine the direction of maximum viscosity in nematic F-actin solutions, and may underestimate the anisotropy in their elastic response. Therefore, further experimental studies on the relation between the microstructure of F-actin and other viscoelastic nematic solutions and their micro- and macroscopic mechanics will greatly benefit from D2PTM.

Because hydrodynamic interactions between distant particles are weak, two-point PTM typically requires a large number of particle tracks in order to achieve statistically converged measurements of cross-correlated particle motion. D2PTM is no exception to this rule, especially for the cross-correlation of particle motion along orthogonal directions (*e.g.* motion of particle α in ∥ direction with motion of particle β in ⊥ direction, see Figs. 7*b*,8*b* and 11*b*). However, proper normalization of the D2PTM equations (33)–(35) can significantly accelerate statistical convergence. Our experiments provide a quantification of the standard deviation of cross-MSD and shear modulus measurements in D2PTM experiments. This quantification could be used in designing future experiments to estimate the number of particle pairs necessary to achieve a given error in the estimation of a sample's mean shear moduli (i.e. the standard error). In the case of our 16 wt%-DSCG, 14 wt%-DSCG and F-actin experiments with 3,315, 816 and 6,105 particle pairs respectively, the errors in the samples' mean shear moduli are expected to be negligible.

The theoretical framework employed here to develop D2PTM is based on a number of simplifications that could potentially limit the applicability of this new microrheology technique. Specifically, we work with a continuum incompressible formulation that assumes

small deformations. Thus, the accuracy of D2PTM is expected to deteriorate in experiments that cause large deformations, for strongly non-linear materials, and for materials that are heterogeneous at the length scale of the distance between particle pairs. It is important to note, however, that these simplifications are common to most if not all existing PTM methods[4]. For materials that are partially compressible[84], the Poisson's ratio should be taken into consideration and the theoretical framework should be modified following an approach similar to that of Levine and Lubensky[15].

An additional important simplification made in this work is that the orientation of the nematic director remains uniform over the length scale of the inter-particle distance. This assumption is reasonable in the present experiments. Actin filaments are externally aligned as part of the sample preparation, and their persistence length ξ_p is approximately twice their total length and 80 times the particle radius. The assumption of uniform nematic orientation can be particularly delicate in the vicinity of the particle due to surface effects[85]. Likewise, when probing polymer solutions with $\xi_p \gg a$ the particle may alter the local orientation of filaments near itself[86]. However, these near-field effects have a negligible influence on the hydrodynamic interaction of pairs of distant particles, and thus the ability of D2PTM to quantify the bulk response of the fluid remains largely unaffected[15]. Furthermore, D2PTM is robust with respect to errors in the direction of the nematic director (see Appendix C).

Distortions of the nematic orientation could be incorporated into the D2PTM analysis by considering static non-uniform nematic fields that include defects near the particle surface[79]. Alternatively, the dynamics of the nematic director could be solved taking into account its Frank elasticity constants[87], or using the Poisson-bracket approach[88]. Nonetheless, these refinements would introduce additional material parameters unknown *a priori*, and a two-particle protocol would be insufficient to determine these new parameters together with the Miesowicz shear moduli.

In conclusion, we have developed a new directional two-point particle tracking microrheology method (D2PTM) that provides important new information about the anisotropic viscoelastic response of nematic complex fluids, which had been unaccessible to currently available microrheology techniques.

A Single-particle response function

This appendix provides the general form of the components of the response function (15) of a particle of radius *a* moving in a directional complex fluid, calculated from the integral (12) making use of equations (10)–(11). The singularities of the response function and its Taylor expansion around the isotropy point are also presented.

The components of the response function of nematic complex fluid with general values of the shear moduli α_1^*, $\widetilde{G}_a$, $\widetilde{G}_b$, and $\widetilde{G}_c$ are

$$s\widetilde{\zeta}_{\parallel} = \frac{8\pi a \widetilde{G}_b B(\overrightarrow{\mu})}{D_+(\overrightarrow{\mu})\frac{\arctan[C_+(\overrightarrow{\mu})]}{C_+(\overrightarrow{\mu})} - D_-(\overrightarrow{\mu})\frac{\arctan[C_-(\overrightarrow{\mu})]}{C_-(\overrightarrow{\mu})}}, \quad (46)$$

$$s\widetilde{\zeta}_{\perp} =$$

$$\frac{8\pi a \widetilde{G}_a \left(\frac{\widetilde{G}_b}{\widetilde{\alpha}_1^*}\right)^2 C_-(\overrightarrow{\mu})8\frac{E_+(\overrightarrow{\mu})}{E_-(\overrightarrow{\mu})}}{\frac{\arctan\left(\sqrt{\widetilde{G}_c/\widetilde{G}_a - 1}\right)}{\sqrt{\widetilde{G}_c/\widetilde{G}_a - 1}} + \frac{1}{B(\overrightarrow{\mu})}\frac{\widetilde{G}_a}{\widetilde{G}_b}\left[\frac{\arctan[C_-(\overrightarrow{\mu})]}{C_-(\overrightarrow{\mu})} - \frac{\arctan[C_+(\overrightarrow{\mu})]}{C_+(\overrightarrow{\mu})}\right]}. \quad (47)$$

where we have used the non-dimensional functions

$$A(\overrightarrow{\mu}) = \frac{\widetilde{\alpha}_1^* + \widetilde{G}_c}{\widetilde{G}_b} - 1,$$

$$B(\overrightarrow{\mu}) = \sqrt{A(\overrightarrow{\mu})^2 + \frac{4\widetilde{\alpha}_1^*}{\widetilde{G}_b}},$$

$$C_+(\overrightarrow{\mu}) = \sqrt{\frac{A(\overrightarrow{\mu}) + B(\overrightarrow{\mu})}{2}},$$

$$C_-(\overrightarrow{\mu}) = \sqrt{\frac{A(\overrightarrow{\mu}) - B(\overrightarrow{\mu})}{2}},$$

$$D_+(\overrightarrow{\mu}) = A(\overrightarrow{\mu}) + 2 + B(\overrightarrow{\mu}),$$

$$D_-(\overrightarrow{\mu}) = A(\overrightarrow{\mu}) + 2 - B(\overrightarrow{\mu}),$$

$$E_+(\overrightarrow{\mu}) = A(\overrightarrow{\mu})D_+(\overrightarrow{\mu}) - 2\left(\frac{\widetilde{G}_c}{\widetilde{G}_b} - 1\right),$$

$$E_-(\overrightarrow{\mu}) = A(\overrightarrow{\mu})D_-(\overrightarrow{\mu}) - 2\left(\frac{\widetilde{G}_c}{\widetilde{G}_b} - 1\right).$$

Equations (46)–(47) degenerate in the limit $B(\overrightarrow{\mu}) \to 0$, which occurs whenever

$$\frac{\widetilde{G}_c}{\widetilde{G}_b} \to \left(1 \pm \sqrt{\frac{-\widetilde{\alpha}_1^*}{\widetilde{G}_b}}\right)^2. \quad (48)$$

In this limit, $C_+ \to C_-$, $D_+ \to D_-$ and $E_+ \to E_-$, and the expressions that determine the two components of the response function (46)–(47) become undefined, although solving the limit yields $s\widetilde{\zeta}_{\parallel} = s\widetilde{\zeta}_{\perp} = 0$. There is a change of sign of $s\widetilde{\zeta}_{\perp}$, when crossing the limit (48) along

the branch associated to the − sign, only when $\tilde{\alpha}_1^* < -\tilde{G}_b$, yielding unphysical negative values of the response function. On the other hand, the sign of the response function does not change along the branch associated to the + sign.

Equations (46)–(47) are singular for $\tilde{\alpha}_1^* = 0$. However, the response function can be calculated, for a complex fluid with $\tilde{\alpha}_1^* = 0$, as the limit

$$s\tilde{\zeta}_\parallel \Big|_{\tilde{\alpha}_1^* = 0} = \frac{4\pi a(\tilde{G}_c - \tilde{G}_b)}{\dfrac{\tilde{G}_c}{\tilde{G}_b} \dfrac{\arctan\left(\sqrt{\tilde{G}_c/\tilde{G}_b - 1}\right)}{\sqrt{\tilde{G}_c/\tilde{G}_b - 1}} - 1}, \quad (49)$$

$$s\tilde{\zeta}_\perp \Big|_{\tilde{\alpha}_1^* = 0} =$$

$$\frac{8\pi a(\tilde{G}_c - \tilde{G}_b)}{1 - \dfrac{\arctan\left(\sqrt{\tilde{G}_c/\tilde{G}_b - 1}\right)}{\sqrt{\tilde{G}_c/\tilde{G}_b - 1}} + \dfrac{\tilde{G}_c - \tilde{G}_b}{\tilde{G}_a} \dfrac{\arctan\left(\sqrt{\tilde{G}_c/\tilde{G}_a - 1}\right)}{\sqrt{\tilde{G}_c/\tilde{G}_a - 1}}}. \quad (50)$$

This response function depends exclusively on the three Miesowicz coefficients, $\tilde{G}_a$, $\tilde{G}_b$ and $\tilde{G}_c$. The physical interpretation of these coefficients is represented graphically in Fig. 14.

For complex fluids that are nearly isotropic, the response function can be approximated by the Taylor expansion of equations (46)–(47) around $\tilde{\alpha}_1^* = 0$ and $\tilde{G}_a = \tilde{G}_b = \tilde{G}_c = \tilde{G}$:

$$\frac{s\tilde{\zeta}_\parallel}{6\pi a\tilde{G}} \approx 1 + \frac{4}{35}\frac{\tilde{\alpha}_1^*}{\tilde{G}} + \frac{4}{5}\left(\frac{\tilde{G}_b}{\tilde{G}} - 1\right) + \frac{1}{5}\left(\frac{\tilde{G}_c}{\tilde{G}} - 1\right), \quad (51)$$

$$\begin{aligned}\frac{s\tilde{\zeta}_\perp}{6\pi a\tilde{G}} &\approx 1 + \frac{3}{70}\frac{\tilde{\alpha}_1^*}{\tilde{G}} + \frac{1}{2}\left(\frac{\tilde{G}_a}{\tilde{G}} - 1\right)\\ &+ \frac{1}{10}\left(\frac{\tilde{G}_b}{\tilde{G}} - 1\right) + \frac{2}{5}\left(\frac{\tilde{G}_c}{\tilde{G}} - 1\right).\end{aligned} \quad (52)$$

Equation (47) is also singular for $\tilde{G}_a = \tilde{G}_c$. However, it presents the limit value:

$$s\widetilde{\zeta}_{\perp}\Big|_{\widetilde{G}_a = \widetilde{G}_c} =$$

$$\frac{8\pi a\widetilde{G}_c\left(\dfrac{\widetilde{G}_b}{\widetilde{\alpha}_1^*}\right)^2 C_-(\vec{\mu}) 8\dfrac{E_+(\vec{\mu})}{E_-(\vec{\mu})}}{1 + \dfrac{1}{B(\vec{\mu})}\dfrac{\widetilde{G}_c}{\widetilde{G}_b}\left[\dfrac{\arctan\left[C_-(\vec{\mu})\right]}{C_-(\vec{\mu})} - \dfrac{\arctan\left[C_+(\vec{\mu})\right]}{C_+(\vec{\mu})}\right]} . \quad (53)$$

Equations (49)–(50) present other singularities, for different combinations of $\widetilde{G}_a$, $\widetilde{G}_b$ and $\widetilde{G}_c$, with finite limits:

$$s\widetilde{\zeta}_{\parallel}\Big|_{\substack{\widetilde{\alpha}_1^* = 0 \\ \widetilde{G}_b = \widetilde{G}_c}} = 6\pi a\widetilde{G}_c, \quad (54)$$

$$s\widetilde{\zeta}_{\perp}\Big|_{\substack{\widetilde{\alpha}_1^* = 0 \\ \widetilde{G}_a = \widetilde{G}_c}} = \frac{8\pi a(\widetilde{G}_c - \widetilde{G}_b)}{2 - \dfrac{\widetilde{G}_b}{\widetilde{G}_c} - \dfrac{\arctan\left(\sqrt{\widetilde{G}_c/\widetilde{G}_b - 1}\right)}{\sqrt{\widetilde{G}_c/\widetilde{G}_b - 1}}}, \quad (55)$$

$$s\widetilde{\zeta}_{\perp}\Big|_{\substack{\widetilde{\alpha}_1^* = 0 \\ \widetilde{G}_a = \widetilde{G}_c}} = \frac{24\pi a(\widetilde{G}_a}{\dfrac{\widetilde{G}_a}{\widetilde{G}_c} + 3\dfrac{\arctan\left(\sqrt{\widetilde{G}_c/\widetilde{G}_a - 1}\right)}{\sqrt{\widetilde{G}_c/\widetilde{G}_a - 1}}}, \quad (56)$$

$$s\widetilde{\zeta}_{\perp}\Big|_{\substack{\widetilde{\alpha}_1^* = 0 \\ \widetilde{G}_a = \widetilde{G}_b = \widetilde{G}_c}} = 6\pi a\widetilde{G}_c. \quad (57)$$

B Two-particle response function

This appendix provides the general form of the components of the hydrodynamic interaction tensor $\widetilde{\overline{\overline{\mathcal{G}}}}(\vec{r}; s)$ (see equation 18) of pairs of distant particles moving in a directional complex fluid, calculated as the inverse Fourier transform of equations (10)–(11) when both particles are located in the same plane $z = 0$. For the sake of completeness, we also provide the Green's function for the pressure, *i.e.* the inverse Fourier transform of (9).

The hydrodynamic interaction tensor in a nematic complex fluid, with general values of the shear moduli $\tilde{\alpha}_1^*, \tilde{G}_a, \tilde{G}_b$ and $\tilde{G}_c$, is given by

$$\left.\frac{\widetilde{\mathcal{G}}_{11}}{s}\right|_{z=0} = \frac{\sqrt{2}}{eb}\left(\frac{d+ex^2}{\sqrt{c-ey^2}} - \frac{d-ex^2}{\sqrt{c+ey^2}}\right), \quad (58)$$

$$\left.\frac{\widetilde{\mathcal{G}}_{12}}{s}\right|_{z=0} = \left.\frac{\tilde{G}_{21}}{s}\right|_{z=0} = \frac{\sqrt{2}}{eb}\frac{x}{y}\left(\sqrt{c+ey^2} - \sqrt{c-ey^2}\right), \quad (59)$$

$$\left.\frac{\widetilde{\mathcal{G}}_{13}}{s}\right|_{z=0} = \left.\frac{\tilde{G}_{31}}{s}\right|_{z=0} = 0, \quad (60)$$

$$\begin{aligned}\left.\frac{\widetilde{\mathcal{G}}_{22}}{s}\right|_{z=0} = \frac{\sqrt{2}}{G_c y^2}&\left[\sqrt{2}\sqrt{x^2 + \frac{G_c}{G_a}y^2}\right.\\ &\left.+\frac{1}{eb}\cdot\left(\frac{m_-}{\sqrt{c-ey^2}} - \frac{m_+}{\sqrt{c+ey^2}}\right)\right],\end{aligned} \quad (61)$$

$$\left.\frac{\widetilde{\mathcal{G}}_{23}}{s}\right|_{z=0} = \left.\frac{\tilde{G}_{32}}{s}\right|_{z=0} = 0, \quad (62)$$

$$\begin{aligned}\left.\frac{\widetilde{\mathcal{G}}_{33}}{s}\right|_{z=0} = \frac{\sqrt{2}}{G_c y^2}&\left[-\frac{\sqrt{2}x^2}{\sqrt{x^2 + \frac{G_c}{G_a}y^2}}\right.\\ &\left.+\frac{b}{e}\cdot\left(\frac{n_+}{\sqrt{c+ey^2}} - \frac{n_-}{\sqrt{c-ey^2}}\right)\right],\end{aligned} \quad (63)$$

where x, y and z are the coordinates of the particle-particle separation in the Cartesian coordinate system defined in Fig. 2, and

$$b(\vec{\mu};\vec{r}) = \sqrt{(\tilde{\alpha}_1^* + \tilde{G}_b + \tilde{G}_c)x^2y^2 + \tilde{G}_b x^4 + \tilde{G}_c y^4},$$

$$c(\vec{\mu};\vec{r}) = (\tilde{\alpha}_1^* + \tilde{G}_b + \tilde{G}_c)y^2 + 2\tilde{G}_b x^2,$$

$$d(\vec{\mu};\vec{r}) = (\tilde{\alpha}_1^* + \tilde{G}_b + \tilde{G}_c)x^2 + 2\tilde{G}_c y^2,$$

$$e(\vec{\mu}) = \sqrt{(\tilde{\alpha}_1^* + \tilde{G}_b + \tilde{G}_c)^2 - 4\tilde{G}_b \tilde{G}_c},$$

$$m_+(\vec{\mu};\vec{r}) = (c - G_b x^2)(d + ex^2 - 2G_c y^2) - 2G_b G_c x^2 y^2,$$

$$m_-(\vec{\mu};\vec{r}) = (c - G_b x^2)(d - ex^2 - 2G_c y^2) - 2G_b G_c x^2 y^2,$$

$$n_+(\vec{\mu};\vec{r}) = \tilde{\alpha}_1^* + \tilde{G}_b + \tilde{G}_c + e,$$

$$n_-(\vec{\mu};\vec{r}) = \tilde{\alpha}_1^* + \tilde{G}_b + \tilde{G}_c - e.$$

It should be noted here that all (58), (59), (61) and (63) depend on $\tilde{G}_b$ and $\tilde{G}_c$, while only (61) and (63) depend on $\tilde{G}_a$. The Green's function for the pressure has the form

$$\tilde{\mathcal{P}}_1 \big|_{z=0} = \frac{2\sqrt{2}x}{eb^3}\left[G_c(3\tilde{G}_b h + ly^4)\left(\frac{1}{\sqrt{c+ey^2}} - \frac{1}{\sqrt{c-ey^2}}\right)\right.$$
$$\left. -G_b\left(\frac{q_-}{(c+ey^2)^{3/2}} - \frac{q_+}{(c-ey^2)^{3/2}}\right)\right], \tag{64}$$

$$\tilde{\mathcal{P}}_2 \big|_{z=0} = \frac{2\sqrt{2}y}{eb^3}\left[G_c(3\tilde{G}_b h + ly^4)\left(\frac{1}{\sqrt{c+ey^2}} - \frac{1}{\sqrt{c-ey^2}}\right)\right.$$
$$\left. -G_b\left(\frac{q_-}{(c+ey^2)^{3/2}} - \frac{q_+}{(c-ey^2)^{3/2}}\right)\right], \tag{65}$$

$$\tilde{\mathcal{P}}_3 \big|_{z=0} = 0, \tag{66}$$

where

$$h(\vec{\mu};\vec{r}) = (\tilde{\alpha}_1^* - \tilde{G}_a + \tilde{G}_b + \tilde{G}_c)x^2y^2 + \tilde{G}_b x^4 + \tilde{G}_c y^4,$$

$$l(\vec{\mu}) = (\tilde{\alpha}_1^* - \tilde{G}_a + \tilde{G}_b + \tilde{G}_c)(\tilde{\alpha}_1^* + \tilde{G}_b + \tilde{G}_c) - 4\tilde{G}_b\tilde{G}_c,$$

$$p(\vec{\mu};\vec{r}) = 2\tilde{G}_c y^2 \Big[(h + 2\tilde{G}_b x^4)(\tilde{\alpha}_1^* + \tilde{G}_b + \tilde{G}_c)$$
$$+ \tilde{G}_c y^2(2\tilde{G}_b x^2 - \tilde{G}_a y^2) \Big],$$

$$q_+(\vec{\mu};\vec{r}) = p + \tilde{G}_b x^6(\tilde{G}_a m_+ + 4\tilde{G}_b\tilde{G}_c),$$

$$q_-(\vec{\mu};\vec{r}) = p + \tilde{G}_b x^6(\tilde{G}_a m_- + 4\tilde{G}_b\tilde{G}_c),$$

For a complex fluid with $\tilde{\alpha}_1^* = 0$, equations (58)–(65) are simplified into:

$$\left.\frac{\widetilde{\mathscr{G}}_{11}}{s}\right|_{\substack{z=0 \\ \tilde{\alpha}_1^*=0}} = \frac{2}{\tilde{G}_b - \tilde{G}_c}\left(\frac{1}{\sqrt{x^2+y^2}} - \frac{\tilde{G}_c}{\tilde{G}_b}\frac{1}{\sqrt{x^2 + \frac{\tilde{G}_c}{\tilde{G}_b}y^2}}\right), \quad (67)$$

$$\left.\frac{\widetilde{\mathscr{G}}_{12}}{s}\right|_{\substack{z=0 \\ \tilde{\alpha}_1^*=0}} = \frac{2}{\tilde{G}_b - \tilde{G}_c}\frac{x}{y}\left(\frac{-1}{\sqrt{x^2+y^2}} + \frac{1}{\sqrt{x^2 + \frac{\tilde{G}_c}{\tilde{G}_b}y^2}}\right), \quad (68)$$

$$\left.\frac{\widetilde{\mathscr{G}}_{22}}{s}\right|_{\substack{z=0 \\ \tilde{\alpha}_1^*=0}} = \frac{2}{\tilde{G}_b - \tilde{G}_c}\frac{x^2}{y^2}\Bigg[\frac{-1}{\sqrt{x^2+y^2}} - \frac{\tilde{G}_b}{\tilde{G}_c}\frac{1}{\sqrt{x^2 + \frac{\tilde{G}_c}{\tilde{G}_b}y^2}}$$
$$+ \frac{1}{x^2}\left(\frac{\tilde{G}_b}{\tilde{G}_c} - 1\right)\sqrt{x^2 + \frac{\tilde{G}_c}{\tilde{G}_a}y^2}\Bigg], \quad (69)$$

$$\left.\frac{\widetilde{\mathscr{G}}_{33}}{s}\right|_{\substack{z=0 \\ \widetilde{\alpha}_1^*=0}} = \frac{2}{\widetilde{G}_b - \widetilde{G}_c}\frac{1}{y^2}\left[-\sqrt{x^2+y^2} + \frac{\widetilde{G}_b}{\widetilde{G}_c}\sqrt{x^2 + \frac{\widetilde{G}_c}{\widetilde{G}_b}y^2}\right.$$

$$\left. - \left(\frac{\widetilde{G}_b}{\widetilde{G}_c}-1\right)\frac{x^2}{\sqrt{x^2+\frac{\widetilde{G}_c}{\widetilde{G}_a}y^2}}\right], \tag{70}$$

$$\left.\widetilde{\mathscr{P}}_1\right|_{\substack{z=0 \\ \widetilde{\alpha}_1^*=0}} = \frac{2x}{\widetilde{G}_b-\widetilde{G}_c}\left(\frac{\widetilde{G}_a-\widetilde{G}_c}{(x^2+y^2)^{3/2}} - \frac{\widetilde{G}_c}{\widetilde{G}_b}\frac{\widetilde{G}_a-\widetilde{G}_b}{\left(x^2+\frac{\widetilde{G}_c}{\widetilde{G}_b}y^2\right)^{3/2}}\right), \tag{71}$$

$$\left.\widetilde{\mathscr{P}}_2\right|_{\substack{z=0 \\ \widetilde{\alpha}_1^*=0}} = \frac{2y}{\widetilde{G}_b-\widetilde{G}_c}\left(\frac{\widetilde{G}_a-\widetilde{G}_c}{(x^2+y^2)^{3/2}} - \frac{\widetilde{G}_c}{\widetilde{G}_b}\frac{\widetilde{G}_a-\widetilde{G}_b}{\left(x^2+\frac{\widetilde{G}_c}{\widetilde{G}_b}y^2\right)^{3/2}}\right). \tag{72}$$

For nearly isotropic complex fluids, the particle-particle interaction can be approximated by its Taylor expansion around $\widetilde{\alpha}_1^* = 0$ and $\widetilde{G}_a = \widetilde{G}_b = \widetilde{G}_c = \widetilde{G}$ as

$$\left.\frac{\widetilde{G}\widetilde{\mathscr{G}}_{11}}{s}\right|_{z=0} \approx \frac{2x^2+y^2}{(x^2+y^2)^{3/2}} - \frac{y^2}{8}\frac{8x^4+4x^2y^2+y^4}{(x^2+y^2)^{7/2}}\frac{\widetilde{\alpha}_1^*}{\widetilde{G}}$$

$$- \frac{1}{4}\frac{8x^4+8x^2y^2+3y^4}{(x^2+y^2)^{5/2}}\left(\frac{\widetilde{G}_b}{\widetilde{G}}-1\right) \tag{73}$$

$$- \frac{y^2}{4}\frac{4x^2+y^2}{(x^2+y^2)^{5/2}}\left(\frac{\widetilde{G}_c}{\widetilde{G}}-1\right),$$

$$\left.\frac{\widetilde{G}\widetilde{\mathscr{G}}_{12}}{s}\right|_{z=0} \approx xy \left[\frac{1}{(x^2+y^2)^{3/2}} - \frac{y^2}{8}\frac{6x^2+y^2}{(x^2+y^2)^{7/2}}\frac{\widetilde{\alpha}_1^*}{\widetilde{G}} \right.$$
$$- \frac{1}{4}\frac{4x^2+y^2}{(x^2+y^2)^{5/2}}\left(\frac{\widetilde{G}_b}{\widetilde{G}}-1\right)$$
$$\left. - \frac{3}{4}\frac{y^2}{(x^2+y^2)^{5/2}}\left(\frac{\widetilde{G}_c}{\widetilde{G}}-1\right) \right], \tag{74}$$

$$\left.\frac{\widetilde{G}\widetilde{\mathscr{G}}_{22}}{s}\right|_{z=0} \approx \frac{x^2+2y^2}{(x^2+y^2)^{3/2}} - \frac{5}{8}\frac{x^2y^4}{(x^2+y^2)^{7/2}}\frac{\widetilde{\alpha}_1^*}{\widetilde{G}}$$
$$- \frac{1}{\sqrt{x^2+y^2}}\left(\frac{\widetilde{G}_a}{\widetilde{G}}-1\right)$$
$$- \frac{3}{4}\frac{x^2y^2}{(x^2+y^2)^{5/2}}\left(\frac{\widetilde{G}_b}{\widetilde{G}}-1\right)$$
$$- \frac{y^2}{4}\frac{x^2+4y^2}{(x^2+y^2)^{5/2}}\left(\frac{\widetilde{G}_c}{\widetilde{G}}-1\right), \tag{75}$$

$$\left.\frac{\widetilde{G}\widetilde{\mathscr{G}}_{33}}{s}\right|_{z=0} \approx \frac{1}{\sqrt{x^2+y^2}} - \frac{1}{8}\frac{y^4}{(x^2+y^2)^{5/2}}\frac{\widetilde{\alpha}_1^*}{\widetilde{G}}$$
$$- \frac{x^2}{(x^2+y^2)^{3/2}}\left(\frac{\widetilde{G}_a}{\widetilde{G}}-1\right)$$
$$- \frac{1}{4}\frac{y^2}{(x^2+y^2)^{3/2}}\left(\frac{\widetilde{G}_b}{\widetilde{G}}-1\right)$$
$$- \frac{3}{4}\frac{y^2}{(x^2+y^2)^{3/2}}\left(\frac{\widetilde{G}_c}{\widetilde{G}}-1\right), \tag{76}$$

$$\left.\widetilde{\mathscr{P}}_1\right|_{z=0} \approx \frac{x}{(x^2+y^2)^{3/2}}\left[2 - \frac{3}{4}\frac{4x^2-y^2}{(x^2+y^2)^2}y^2\frac{\widetilde{\alpha}_1^*}{\widetilde{G}} \right.$$
$$\left. + \frac{2x^2-y^2}{x^2+y^2}\left(\frac{\widetilde{G}_a}{\widetilde{G}}-1\right) + \frac{2x^2-y^2}{x^2+y^2}\left(\frac{\widetilde{G}_b}{\widetilde{G}}-1\right) \right], \tag{77}$$

$$\widetilde{\mathscr{P}}_2\Big|_{z=0} \approx \frac{y}{(x^2+y^2)^{3/2}}\Bigg[2 - \frac{3}{4}\frac{4x^2-y^2}{(x^2+y^2)^2}y^2\frac{\widetilde{\alpha}_1^*}{\widetilde{G}}$$
$$+ \frac{2x^2-y^2}{x^2+y^2}\left(\frac{\widetilde{G}_a}{\widetilde{G}}-1\right) + \frac{2x^2-y^2}{x^2+y^2}\left(\frac{\widetilde{G}_b}{\widetilde{G}}-1\right)\Bigg]. \tag{78}$$

Equations (58)–(65) are also singular for other combinations of the viscoelasticity parameters. Here we list their limit values. For $\widetilde{\alpha}_1^* = \widetilde{\alpha} = -\left(\sqrt{\widetilde{G}_b} - \sqrt{\widetilde{G}_c}\right)^2$, we have:

$$\frac{\widetilde{\mathscr{G}}_{11}}{s}\Bigg|_{\substack{z=0 \\ \widetilde{\alpha}_1^*=\widetilde{\alpha}}} = \frac{1}{\widetilde{G}_b}\frac{2x^2+\sqrt{\dfrac{\widetilde{G}_c}{\widetilde{G}_b}}y^2}{\left(x^2+\sqrt{\dfrac{\widetilde{G}_c}{\widetilde{G}_b}}y^2\right)^{3/2}}, \tag{79}$$

$$\frac{\widetilde{\mathscr{G}}_{12}}{s}\Bigg|_{\substack{z=0 \\ \widetilde{\alpha}_1^*=\widetilde{\alpha}}} = \frac{1}{\widetilde{G}_b}\frac{xy}{\left(x^2+\sqrt{\dfrac{\widetilde{G}_c}{\widetilde{G}_b}}y^2\right)^{3/2}}, \tag{80}$$

$$\frac{\widetilde{\mathscr{G}}_{22}}{s}\Bigg|_{\substack{z=0 \\ \widetilde{\alpha}_1^*=\widetilde{\alpha}}} = \frac{1}{\widetilde{G}_c y^2}\left(2\sqrt{x^2+\frac{\widetilde{G}_c}{\widetilde{G}_a}y^2} - x^2\frac{2x^2+3\sqrt{\dfrac{\widetilde{G}_c}{\widetilde{G}_b}}y^2}{\left(x^2+\sqrt{\dfrac{\widetilde{G}_c}{\widetilde{G}_b}}y^2\right)^{3/2}}\right), \tag{81}$$

$$\frac{\widetilde{\mathscr{G}}_{33}}{s}\Bigg|_{\substack{z=0 \\ \widetilde{\alpha}_1^*=\widetilde{\alpha}}} = \frac{1}{\widetilde{G}_c y^2}\left(\frac{-2x^2}{\sqrt{x^2+\dfrac{\widetilde{G}_c}{\widetilde{G}_a}y^2}} + \frac{2x^2+\sqrt{\dfrac{\widetilde{G}_c}{\widetilde{G}_b}}y^2}{\sqrt{x^2+\sqrt{\dfrac{\widetilde{G}_c}{\widetilde{G}_b}}y^2}}\right), \tag{82}$$

$$\widetilde{\mathscr{P}}_1 \Big|_{\substack{z=0 \\ \widetilde{\alpha}_1^* = \widetilde{\alpha}}} = \frac{x}{\widetilde{G}_b \left(x^2 + \sqrt{\frac{\widetilde{G}_c}{\widetilde{G}_b}} y^2 \right)^{5/2}} \Bigg[$$

$$3\widetilde{G}_c y^2 + \widetilde{G}_a \sqrt{\frac{\widetilde{G}_c}{\widetilde{G}_b}} y^2 \frac{5x^4 - \frac{\widetilde{G}_c}{\widetilde{G}_b} y^4}{\left(x^2 + \sqrt{\frac{\widetilde{G}_c}{\widetilde{G}_b}} y^2 \right)^2} \qquad (83)$$

$$+ 2\widetilde{G}_a x^4 \frac{x^4 - \frac{\widetilde{G}_c}{\widetilde{G}_b} y^4}{\left(x^2 + \sqrt{\frac{\widetilde{G}_c}{\widetilde{G}_b}} y^2 \right)^3} \Bigg],$$

$$\widetilde{\mathscr{P}}_2 \Big|_{\substack{z=0 \\ \widetilde{\alpha}_1^* = \widetilde{\alpha}}} = \frac{y}{\widetilde{G}_b \left(x^2 + \sqrt{\frac{\widetilde{G}_c}{\widetilde{G}_b}} y^2 \right)^{5/2}} \Bigg[$$

$$3\widetilde{G}_c y^2 + \widetilde{G}_a \sqrt{\frac{\widetilde{G}_c}{\widetilde{G}_b}} y^2 \frac{5x^4 - \frac{\widetilde{G}_c}{\widetilde{G}_b} y^4}{\left(x^2 + \sqrt{\frac{\widetilde{G}_c}{\widetilde{G}_b}} y^2 \right)^2} \qquad (84)$$

$$+ 2\widetilde{G}_a x^4 \frac{x^4 - \frac{\widetilde{G}_c}{\widetilde{G}_b} y^4}{\left(x^2 + \sqrt{\frac{\widetilde{G}_c}{\widetilde{G}_b}} y^2 \right)^3} \Bigg].$$

For $\widetilde{\alpha}_1^* = \widetilde{\alpha} = -\left(\sqrt{\widetilde{G}_b} - \sqrt{\widetilde{G}_c} \right)^2$:

$$\frac{\widetilde{\mathscr{G}}_{11}}{s} \Big|_{\substack{z=0 \\ \widetilde{\alpha}_1^* = \widetilde{\alpha}}} = \frac{1}{\widetilde{G}_b} \frac{2x^2 - \sqrt{\frac{\widetilde{G}_c}{\widetilde{G}_b}} y^2}{\left(x^2 - \sqrt{\frac{\widetilde{G}_c}{\widetilde{G}_b}} y^2 \right)^{3/2}}, \qquad (85)$$

$$\frac{\widetilde{\mathcal{G}}_{12}}{s}\bigg|_{\substack{z=0 \\ \tilde{\alpha}_1^* = \tilde{\alpha}}} = \frac{1}{\widetilde{G}_b} \frac{xy}{\left(x^2 - \sqrt{\frac{\widetilde{G}_c}{\widetilde{G}_b}}y^2\right)^{3/2}}, \quad (86)$$

$$\frac{\widetilde{\mathcal{G}}_{22}}{s}\bigg|_{\substack{z=0 \\ \tilde{\alpha}_1^* = \tilde{\alpha}}} = \frac{1}{\widetilde{G}_c y^2}\left(2\sqrt{x^2 + \frac{\widetilde{G}_c}{\widetilde{G}_a}y^2}\right.$$

$$\left. -x^2\frac{2x^2 - 3\sqrt{\frac{\widetilde{G}_c}{\widetilde{G}_b}}y^2}{\left(x^2 - \sqrt{\frac{\widetilde{G}_c}{\widetilde{G}_b}}y^2\right)^{3/2}}\right), \quad (87)$$

$$\frac{\widetilde{\mathcal{G}}_{33}}{s}\bigg|_{\substack{z=0 \\ \tilde{\alpha}_1^* = \tilde{\alpha}}} = \frac{1}{\widetilde{G}_c y^2}\left(\frac{-2x^2}{\sqrt{x^2 + \frac{\widetilde{G}_c}{\widetilde{G}_a}y^2}}\right.$$

$$\left. + \frac{2x^2 - \sqrt{\frac{\widetilde{G}_c}{\widetilde{G}_b}}y^2}{\sqrt{x^2 - \sqrt{\frac{\widetilde{G}_c}{\widetilde{G}_b}}y^2}}\right), \quad (88)$$

$$\widetilde{\mathscr{P}}_1 \Big|_{\substack{z=0 \\ \widetilde{\alpha}_1^* = \widetilde{\alpha}}} = \frac{x}{\widetilde{G}_b \left(x^2 - \sqrt{\frac{\widetilde{G}_c}{\widetilde{G}_b}} y^2 \right)^{5/2}} \Big[$$

$$3\widetilde{G}_c y^2 - \widetilde{G}_a \sqrt{\frac{\widetilde{G}_c}{\widetilde{G}_b}} y^2 \frac{5x^4 - \frac{\widetilde{G}_c}{\widetilde{G}_b} y^4}{\left(x^2 - \sqrt{\frac{\widetilde{G}_c}{\widetilde{G}_b}} y^2 \right)^2} \qquad (89)$$

$$+ 2\widetilde{G}_a x^4 \frac{x^4 - \frac{\widetilde{G}_c}{\widetilde{G}_b} y^4}{\left(x^2 - \sqrt{\frac{\widetilde{G}_c}{\widetilde{G}_b}} y^2 \right)^3} \Big],$$

$$\widetilde{\mathscr{P}}_2 \Big|_{\substack{z=0 \\ \widetilde{\alpha}_1^* = \widetilde{\alpha}}} = \frac{y}{\widetilde{G}_b \left(x^2 - \sqrt{\frac{\widetilde{G}_c}{\widetilde{G}_b}} y^2 \right)^{5/2}} \Big[$$

$$3\widetilde{G}_c y^2 - \widetilde{G}_a \sqrt{\frac{\widetilde{G}_c}{\widetilde{G}_b}} y^2 \frac{5x^4 - \frac{\widetilde{G}_c}{\widetilde{G}_b} y^4}{\left(x^2 - \sqrt{\frac{\widetilde{G}_c}{\widetilde{G}_b}} y^2 \right)^2} \qquad (90)$$

$$+ 2\widetilde{G}_a x^4 \frac{x^4 - \frac{\widetilde{G}_c}{\widetilde{G}_b} y^4}{\left(x^2 - \sqrt{\frac{\widetilde{G}_c}{\widetilde{G}_b}} y^2 \right)^3} \Big].$$

When $\widetilde{\alpha}_1^* = 0$ and $\widetilde{G}_b = \widetilde{G}_c$:

$$\frac{\widetilde{\mathscr{G}}_{11}}{s} \Big|_{\substack{z=0 \\ \widetilde{G}_b = \widetilde{G}_c}} = \frac{1}{\widetilde{G}_c} \frac{2x^2 + y^2}{(x^2 + y^2)^{3/2}}, \quad (91)$$

$$\frac{\widetilde{\mathscr{G}}_{12}}{s} \Big|_{\substack{z=0 \\ \widetilde{G}_b = \widetilde{G}_c}} = \frac{1}{\widetilde{G}_c} \frac{xy}{(x^2 + y^2)^{3/2}}, \quad (92)$$

$$\left.\frac{\widetilde{\mathscr{G}}_{22}}{s}\right|_{\substack{z=0 \\ \tilde{G}_b = \tilde{G}_c}} = \frac{1}{\tilde{G}_c y^2}\left(2\sqrt{x^2 + \frac{\tilde{G}_c}{\tilde{G}_a}y^2} - x^2\frac{2x^2 + 3y^2}{(x^2 + y^2)^{3/2}}\right), \quad (93)$$

$$\left.\frac{\widetilde{\mathscr{G}}_{33}}{s}\right|_{\substack{z=0 \\ \tilde{G}_b = \tilde{G}_c}} = \frac{1}{\tilde{G}_c y^2}\left(\frac{2x^2 + y^2}{\sqrt{x^2 + y^2}} - \frac{2x^2}{\sqrt{x^2 + \frac{\tilde{G}_c}{\tilde{G}_a}y^2}}\right), \quad (94)$$

$$\left.\widetilde{\mathscr{P}}_1\right|_{\substack{z=0 \\ \tilde{G}_b = \tilde{G}_c}} = \frac{x\left[2\tilde{G}_a + 3(\tilde{G}_c - \tilde{G}_a)\frac{y^2}{x^2 + y^2}\right]}{\tilde{G}_c(x^2 + y^2)^{3/2}}, \quad (95)$$

$$\left.\widetilde{\mathscr{P}}_2\right|_{\substack{z=0 \\ \tilde{G}_b = \tilde{G}_c}} = \frac{y\left[2\tilde{G}_a + 3(\tilde{G}_c - \tilde{G}_a)\frac{y^2}{x^2 + y^2}\right]}{\tilde{G}_c(x^2 + y^2)^{3/2}}. \quad (96)$$

When $\tilde{\alpha}_1^* = 0$ and $\tilde{G}_a = \tilde{G}_b = \tilde{G}_c$:

$$\left.\frac{\widetilde{\mathscr{G}}_{22}}{s}\right|_{\substack{z=0 \\ \tilde{G}_a = \tilde{G}_b = \tilde{G}_c}} = \frac{1}{\tilde{G}_c}\frac{x^2 + 2y^2}{(x^2 + y^2)^{3/2}}, \quad (97)$$

$$\left.\frac{\widetilde{\mathscr{G}}_{33}}{s}\right|_{\substack{z=0 \\ \tilde{G}_a = \tilde{G}_b = \tilde{G}_c}} = \frac{1}{\tilde{G}_c}\frac{1}{\sqrt{x^2 + y^2}}, \quad (98)$$

$$\left.\widetilde{\mathscr{P}}_1\right|_{\substack{z=0 \\ \tilde{G}_a = \tilde{G}_b = \tilde{G}_c}} = \frac{2x}{(x^2 + y^2)^{3/2}}, \quad (99)$$

$$\left.\widetilde{\mathscr{P}}_2\right|_{\substack{z=0 \\ \widetilde{G}_a = \widetilde{G}_b = \widetilde{G}_c}} = \frac{2y}{(x^2 + y^2)^{3/2}}. \quad (100)$$

Another singularity arises when $y = 0$, independently of the viscoelasticity coefficients:

$$\left.\frac{\widetilde{\mathscr{G}}_{12}}{s}\right|_{\substack{z=0 \\ y=0}} = 0, \quad (101)$$

$$\left.\frac{\widetilde{\mathscr{G}}_{22}}{s}\right|_{\substack{z=0 \\ y=0}} = \frac{1}{\widetilde{G}_a x}, \quad (102)$$

$$\left.\frac{\widetilde{\mathscr{G}}_{33}}{s}\right|_{\substack{z=0 \\ y=0}} = \frac{1}{\widetilde{G}_a x}. \quad (103)$$

C Influence of the uncertainty in the determination of the director

Prior to calculating directional shear moduli, it is necessary to determine the orientation of the nematic director $\overrightarrow{n}$ from the principal directions of the MSD matrix (see §2.5). This process adds a potential source of error on top of the error associated to the value of the principal MSDs. To quantify how errors in the orientation of $\overrightarrow{n}$ may affect the measured velocity Green's function, $\widetilde{\mathscr{G}}_{ij}^*$, we calculate the deviation $\Delta\widetilde{\mathscr{G}}_{ij} = \widetilde{\mathscr{G}}_{ij}^* - \widetilde{\mathscr{G}}_{ij}$ of this function from its exact value $\widetilde{\mathscr{G}}_{ij}$, when the orientation of $\overrightarrow{n}$ has an error $\Delta\theta$.

We consider a nematic complex fluid, and a coordinate system where x is aligned with the director. Two particles, α and β are located, respectively, at the origin and at a location (x, y). The plane $z = 0$ is defined by the location of the particles and the director $\overrightarrow{n}$ as in §2.3. In polar coordinates, the particle β is located at (R, θ), where R is the distance between the particles, and θ is the angle between $\overrightarrow{n}$ and the line that connects both particles. Consistent with our D2PTM formulation, we examine the case $\tilde{\alpha}_1^* = 0$, for which $\widetilde{\mathscr{G}}_{ij}$ is given in (67)–(72). We focus on the components of the Green's function used in eqs. (33)–(35) to determine the Miesowicz shear moduli, and we keep the normalization used in those equations (*i.e.* $\frac{y}{x}\widetilde{\mathscr{G}}_{12}$ instead of $\widetilde{\mathscr{G}}_{12}$). Up to first order in $\Delta\theta$, the relative error of these components is

$$
\left.\frac{\Delta\widetilde{\mathscr{G}}_{11}}{\widetilde{\mathscr{G}}_{11}}\right|_{\substack{z=0\\ \tilde{\alpha}_1^*=0}} =
$$

$$
= \frac{\dfrac{\tilde{G}_c}{\tilde{G}_b}\left(1-\dfrac{\tilde{G}_c}{\tilde{G}_b}\right)\sin\theta\cos\theta}{\left(\cos^2\theta+\dfrac{\tilde{G}_c}{\tilde{G}_b}\sin^2\theta\right)\left(\dfrac{\tilde{G}_c}{\tilde{G}_b}-\sqrt{\cos^2\theta+\dfrac{\tilde{G}_c}{\tilde{G}_b}\sin^2\theta}\right)}\Delta\theta,
\tag{104}
$$

$$
\left.\frac{\Delta\left(\frac{y}{x}\widetilde{\mathscr{G}}_{12}\right)}{\frac{y}{x}\widetilde{\mathscr{G}}_{12}}\right|_{\substack{z=0\\ \tilde{\alpha}_1^*=0}} =
$$

$$
= \frac{\left(1-\dfrac{\tilde{G}_c}{\tilde{G}_b}\right)\sin\theta\cos\theta}{\left(\cos^2\theta+\dfrac{\tilde{G}_c}{\tilde{G}_b}\sin^2\theta\right)\left(1-\sqrt{\cos^2\theta+\dfrac{\tilde{G}_c}{\tilde{G}_b}\sin^2\theta}\right)}\Delta\theta,
\tag{105}
$$

$$
\left.\frac{\Delta\widetilde{\mathscr{G}}_{22}}{\widetilde{\mathscr{G}}_{22}}\right|_{\substack{z=0\\ \tilde{\alpha}_1^*=0}} =
$$

$$
= \frac{\left(\dfrac{\tilde{G}_b}{\tilde{G}_c}-1\right)\dfrac{\sin\theta}{\cos\theta}\Delta\theta}{1-\dfrac{\dfrac{\tilde{G}_b}{\tilde{G}_c}}{\sqrt{\cos^2\theta+\dfrac{\tilde{G}_c}{\tilde{G}_b}\sin^2\theta}}+\dfrac{\left(\dfrac{\tilde{G}_b}{\tilde{G}_c}-1\right)\sqrt{\cos^2\theta+\dfrac{\tilde{G}_c}{\tilde{G}_a}\sin^2\theta}}{\cos^2\theta}}\cdot\Bigg(
$$

$$
-\frac{\cos^2\theta}{\left(\cos^2\theta+\dfrac{\tilde{G}_c}{\tilde{G}_b}\sin^2\theta\right)^{3/2}}+2\frac{\sqrt{\cos^2\theta+\dfrac{\tilde{G}_c}{\tilde{G}_a}\sin^2\theta}}{\cos^2\theta}-
$$

$$
\frac{1-\dfrac{\tilde{G}_c}{\tilde{G}_a}}{\sqrt{\cos^2\theta+\dfrac{\tilde{G}_c}{\tilde{G}_a}\sin^2\theta}}\Bigg)-\frac{2\Delta\theta}{\cos\theta\sin\theta}\,.
\tag{106}
$$

We focus on the *quasi-isotropic* limit (*i.e.* when $\widetilde{G}_a \approx \widetilde{G}_b \approx \widetilde{G}_c$), in which the uncertainty in the determination of the nematic director is expected to be highest. The relative error in this limit is

$$\frac{\Delta(\widetilde{\mathscr{G}}_{11})}{(\widetilde{\mathscr{G}}_{11})}\bigg|_{\substack{z=0 \\ \tilde{\alpha}_1^*=0}} \rightarrow -\frac{2\sin\theta\cos\theta}{1+\cos^2\theta}\Delta\theta,$$

$$\frac{\Delta\left(\frac{y}{x}\widetilde{\mathscr{G}}_{12}\right)}{\left(\frac{y}{x}\widetilde{\mathscr{G}}_{12}\right)}\bigg|_{\substack{z=0 \\ \tilde{\alpha}_1^*=0}} \rightarrow 2\cot\theta\Delta\theta, \qquad (107)$$

$$\frac{\Delta(\widetilde{\mathscr{G}}_{22})}{(\widetilde{\mathscr{G}}_{22})}\bigg|_{\substack{z=0 \\ \tilde{\alpha}_1^*=0}} \rightarrow \frac{2\sin\theta\cos\theta}{1+\sin^2\theta}\Delta\theta.$$

As expected, the relative error in $\widetilde{\mathscr{G}}_{22}$ in the quasi-isotropic limit is related to the error in $\widetilde{\mathscr{G}}_{11}$ by a rotation $\theta \rightarrow \theta + \pi/2$. The leading order factor in both errors is bound by 0.71, so that the errors remain small and of order $\Delta\theta$. The relative error of $\frac{y}{x}\widetilde{\mathscr{G}}_{12}$ becomes singular near the nematic axis $\theta = 0$. However, it is important to note that $\frac{y}{x}\widetilde{\mathscr{G}}_{12} \sim \sin^2\theta$ near the nematic axis in the quasi-isotropic limit. Thus, the absolute contributions to the error coming from this component of the Green's function are in fact negligible near the nematic axis.

In conclusion, this analysis suggest that deviations in the orientation of the nematic director cause small relative errors in the equations (33)–(35) used to determine the Miesowicz shear moduli.

D Validation of D2PTM

D.1 D2PTM of disodium cromoglycate (DSCG). Additional data

Fig. 15 displays the MSDs measured for microrheological probes immersed in a 14% wt nematic DSCG solution. Both the one-point and two-point MSDs are qualitatively similar to the results obtained for the 16% wt solution (see Fig. 7 in the main text). Furthermore, the Miesowicz viscosity coefficients determined from these MSDs are in good agreement with Zhou *et al.* 's[52] results (see Table 1).

D.2 Validation of D2PTM by Numerical Simulation. Additional data

The parameters used in the simulation presented in §4.2 were deliberately chosen so that the MSD would display isotropic features at high frequencies and anisotropic characteristics at low frequencies, and thus illustrate the applicability of D2PTM to differentiate these two behaviors. Here, we present additional validation data for a more generic example fluid where the 6 viscoelastic parameters are different from each other, *i.e.* μ_a, = 0.1 Pa, μ_b = 0.4

Pa, $\mu_c = 0.3$ Pa, $\eta_a = 0.6$ Pa·s, $\eta_b = 0.2$ Pa·s and $\eta_c = 0.4$ Pa·s, and show that they can also be recovered by D2PTM (Fig. 16).

E Validation of the particle tracking setup

To characterize the accuracy of the imaging platform and particle tracking algorithm implemented for our experiments, we performed PTM in a solution of glycerol and water, which is a well characterized system with isotropic Newtonian rheology. We prepared control isotropic samples of 50% (v/v) glycerol in water, which results in a bulk viscosity consistent with MSD values that span the range of MSD measured in the F-actin experiments.

Fig. 17 shows the MSD of the probing particles in principal directions as well as the total MSD. For the whole range of representative frequencies of the experiment, the MSD follow a straight line with unit slope down to the lowest values of τ. This result indicates that our particle tracking setup has sufficient spatial resolution to track particle displacements at our experimental sampling frequency. Furthermore, we calculated the viscosity of the sample from the MSD by applying standard PTM (equation 28), and obtained a viscosity coefficient of $\eta \approx 6.5$ mPa·s, consistent with a 50% (v/v) solution of glycerol in water, at 20°C. Another important result stemming from Fig. 17 is that, although the isotropic samples were confined in the same capillary tubes than the F-actin solutions, the measured MSD are isotropic up to time separations $\tau \sim 10s$. Thus, the spatial confinement induced by the walls of the capillary tube does not induce anisotropic particle mobility in the range of frequencies of interest.

F List of symbols

Due to the high mathematical content of this article, here we present a small summary of the most relevant mathematical symbols used.

MSD: Mean Squared Displacements.

G: Shear modulus.

ω: Frequency.

G': Storage modulus.

G'': Loss modulus.

a: Particle radius.

F, f: Forces.

ρ: Density.

v: Velocity.

τ_{ij}: Stress tensor.

e_{ij}: Shear strain tensor.

∂_t: Partial derivative with respect to t.

u: Displacement.

η: Viscosity coefficient.

$\tilde{}$: Laplace transform.

p: Pressure.

α_i: Leslie coefficients.

i, j, k and q: Counters.

s: Laplace complex frequency.

$\vec{n}$: Director of the nematic.

$\vec{N}$: Rate of change of the director with respect to the background fluid.

$\tilde{G}_a$, $\tilde{G}_b$ and $\tilde{G}_c$: Generalized Miesowicz shear moduli.

x, y and z: Space coordinates.

∂_x, ∂_y and ∂_z: Partial derivatives with respect to the space coordinates.

$\vec{r}$: Vector position.

ζ: Hydrodynamic resistance of a particle.

$\widehat{\mathscr{G}}_{ij}$: Greens function for the velocity.

$\widehat{\mathscr{P}}_j$: Greens function for the pressure.

$\hat{}$: Fourier transform along the space coordinates.

k_j: Space wavenumbers.

α: Particle identifier.

β: Particle identifier.

$\vec{r}_{\alpha,\beta}$: Vector separation between particles.

$\mathscr{L}$: Multiparticle resistance tensor.

k_B: Boltzmann constant.

T: Absolute temperature.

τ: Time step.

$\Delta x(\tau)$: Particle jump, in the coordinate *x*, during time τ.

eff: Effective.

∥: Direction parallel to the nematic director.

⊥: Direction perpendicular to the nematic director.

$\langle ... \rangle$: Ensemble average.

Σ: Covariance matrix of a random distribuion.

Acknowledgements

References

1. Mason TG and Weitz DA, Physical Review Letters, 1995, 74, 1250–1253. [PubMed: 10058972]

2. Mason TG, Ganesan K, van Zanten JH, Wirtz D and Kuo SC, Physical Review Letters, 1997, 79, 3282–3285.

3. Wirtz D, Annual review of biophysics, 2009, 38, 301–326.

4. Squires TM and Mason TG, Annual Review of Fluid Mechanics, 2010, 42, 413–438.

5. Carpen IC and Brady JF, Journal of Rheology (1978-present), 2005, 49, 1483–1502.

6. Meyer A, Marshall A, Bush BG and Furst EM, Journal of Rheology (1978-present), 2006, 50, 77–92.

7. Wilson L, Harrison A, Schofield A, Arlt J and Poon W, The Journal of Physical Chemistry B, 2009, 113, 3806–3812. [PubMed: 19673070]

8. Amblard F, Maggs AC, Yurke B, Pargellis AN and Leibler S, Physical Review Letters, 1996, 77, 4470–4473. [PubMed: 10062546]

9. Gittes F, Schnurr B, Olmsted PD, MacKintosh FC and Schmidt CF, Physical Review Letters, 1997, 79, 3286–3289.

10. Mizuno D, Head D, MacKintosh F and Schmidt C, Macromolecules, 2008, 41, 7194–7202.

11. Tseng Y, Kole TP and Wirtz D, Biophysical Journal, 2002, 83, 3162–3176. [PubMed: 12496086]

12. del Álamo JC, Norwich GN, Li YJ, Lasheras JC and Chien S, Proceedings of the National Academy of Sciences of the United States of America, 2008, 105, 15411–15416. [PubMed: 18840694]

13. Guo M, Ehrlicher AJ, Jensen MH, Renz M, Moore JR, Goldman RD, Lippincott-Schwartz J, Mackintosh FC and Weitz DA, Cell, 2014, 158, 822–832. [PubMed: 25126787]

14. Fu HC, Shenoy VB and Powers TR, Physical Review E, 2008, 78, 061503.

15. Levine AJ and Lubensky TC, Physical Review E, 2001, 63, 041510.

16. Valentine MT, Perlman ZE, Gardel ML, Shin JH, Matsudaira P, Mitchison TJ and Weitz DA, Biophysical Journal, 2004, 86, 4004–4014. [PubMed: 15189896]

17. Crocker JC, Valentine MT, Weeks ER, Gisler T, Kaplan PD, Yodh AG and Weitz DA, Physical Review Letters, 2000, 85, 888–891 [PubMed: 10991424]

18. Loudet JC, Hanusse P and Poulin P, Science, 2004, 306, 1525–1525. [PubMed: 15567855]

19. Turiv T, Lazo I, Brodin A, Lev BI, Reiffenrath V, Nazarenko VG and Lavrentovich OD, Science, 2013, 342, 1351–1354. [PubMed: 24337292]

20. Hasnain IA and Donald AM, Physical Review E, 2006, 73, 031901.

21. He J, Mak M, Liu Y and Tang JX, Physical Review E, 2008, 78, 011908.

22. Osterday K, Chew T, Loury P, Haga J, Gomez-Gonzalez M, del Alamo JC and Chien S, arXiv preprint arXiv:1309.2683, 2013.

23. Lee H-H, Lee H-C, Chou C-C, Hur SS, Osterday K, del Álamo JC, Lasheras JC and Chien S, Proceedings of the National Academy of Sciences, 2013, 110, 2840–2845.

24. Chen Y-Q, Su P-T, Chen Y-H, Wei M-T, Huang C-H, Osterday K, del Álamo JC, Syu W-J and Chiou A, PloS one, 2014, 9, e112137. [PubMed: 25369259]

25. Mak M, Kamni RD and Zaman MH, PLoS computational biology, 2014, 10, e1003959. [PubMed: 25412385]

26. Gómez-González M and del Álamo JC, Journal of Fluid Mechanics, 2013, 725, 299–331

27. Landau LD and Lifshitz EM, Fluid Mechanics, Pergamon Press, Second English edn, 1987, vol. 6.

28. Levine AJ and Lubensky TC, Physical Review Letters, 2000, 85, 1774–1777. [PubMed: 10970611]

29. Su J, Jiang X, Welsch R, Whitesides GM and So PTC, Molecular & Cellular Biomechanics, 2007, 4, 87–104. [PubMed: 17937113]

30. Schnurr B, Gittes F, MacKintosh FC and Schmidt CF, Macromolecules, 1997, 30, 7781–7792.

31. Ericksen JL, Archive for Rational Mechanics and Analysis, 1960, 4, 231–237.

32. Leslie FM, Quarterly Journal of Mechanics and Applied Mathematics, 1966, 19, 357–370.

33. De Gennes PG and Prost J, The Physics of Liquid Crystals, Oxford University Press, 2nd edn, 1993.

34. Miesowicz M, Bulletin International de l'Acaclémie Polonaise des Sciences etdes Lettres, 1936, 228–247.

35. Parodi O, Le Journal de Physique, 1970, 31, 581–584.

36. Simões M and Domiciano SM, Physical Review E, 2002, 061703.

37. Kim S and Karrila SJ, Microhydrodynamics - Principles and Selected Applications, Dover Publications, Inc., 2005.

38. Squires TM and Mason TG, Rheologica Acta, 2010, 49, 1165–1177.

39. Liron N and Barta E, Journal of Fluid Mechanics, 1992, 238, 579–598.

40. Ladyzhenskaya OA, The Mathematical Theoiy of Viscous Incompressible Flow, Gordon and Breach Science Publishers, Second English edn, 1969.

41. Beale JT and Lai M-C, SIAM Journal on Numerical Analysis, 2001, 38, 1902–1925.

42. Cortez R, SIAM Journal on Scientific Computing, 2001, 23, 1204–1225.

43. Tseng HC, Silver DL and Finlayson BA, The Physics of fluids, 1972, 15, 1213–1222.

44. Gähwiller C, Physics Letters A, 1971, 36, 311–312.

45. Herba H, Szymanski A and Drzymala A, Molecular Ctystals and Liquid Ctystals, 1985, 127, 153–158.

46. Wang H, Wu TX, Gauza S, Wu JR and Wu S-T, Liquid ctystals, 2006, 33, 91–98.

47. Beens WW and de Jeu WH, Journal de physique, 1983, 44, 129–136.

48. Tassieri M, Evans RML, Warren RL, Bailey NJ and Cooper JM, New Journal of Physics, 2012, 115032.

49. Pardee JD and Spudich JA, Methods in Enzymology, 1982, 85, 164–181. [PubMed: 7121269]

50. Gittes F, Mickey B, Nettleton J and Howard J, Journal of Cell Biology, 1993, 120, 923–934. [PubMed: 8432732]

51. Mushenheim PC, Trivedi RR, Weibel DB and Abbott NL, Biophysical Journal, 2014, 107, 255–265. [PubMed: 24988359]

52. Zhou S, Neupane K, Nastishin YA, Baldwin AR, Shiyanovskii SV, Lavrentovich OD and Sprunt S, Soft Matter, 2014, 10, 6571–6581. [PubMed: 25043812]

53. http://www.micro-manager.org/.

54. Stuurman N, Amdodaj N and Vale R, Microscopy Today, 2007, 15, 42–43.

55. Edelstein A, Amodaj N, Hoover K, Vale R and Stuurman N, Current Protocols in Molecular Biology, 2010, 14.20.1–14.20.17. [PubMed: 20583094]

56. Parthasarathy R, Nature Methods, 2012, 9, 724–726. [PubMed: 22688415]

57. Kubo R, Reports on progress in physics, 1966, 29, 255–284.

58. Nyquist H, Physical Review, 1928, 32, 110–113.

59. Mörters P and Peres Y, Brownian Motion, Cambridge University Press, 2010.

60. Python Software Foundation, https://www.python.org.

61. van der Walt S, Colbert SC and Varoquaux G, Computing in Science & Engineering, 2011, 13, 22–30.

62. Jones E, Oliphant T, Peterson P et al., SciPy: Open source scientific tools for Python, 2001–, http://www.scipy.org/.

63. Hunter JD, Computing in Science & Engineering, 2007, 90–95.

64. Behnel S, Bradshaw R, Citro C, Dalcin L, Seljebotn DS and Smith K, Computing in Science & Engineering, 2011, 31–39.

65. Laid M, https://github.com/strohel/Ceygen.

66. Inoue H, Kamibayashi M, Kishimoto K, Shibuya T and Koizumi T, JSME International Journal Series 1 - Solid Mechanics Strength of Materials. 1992 35 319–324.

67. Frigo M and Johnson SG, http://www.fftw.org.

68. Frigo M and Johnson SG, Proceedins of the IEEE, 2005, 93, 216–231.

69. Gómez-González M, PhD thesis, University of California San Diego, 2015.

70. Talbot A, Journal of the Institute of Mathematics and its Applications, 1979, 23, 97–120.

71. Weideman JAC, SIAM Journal on Numerical Analysis, 2006, 44, 2342–2362.

72. Dingfelder B and Weideman JAC, Numerical Algorithms, 2015, 68, 167–183.

73. Lydon J, Journal of Materials Chemistry, 2010, 20, 10071–10099.

74. Duchesne I, Rainville S and Galstian T, Biophysical Journal, 2015, 109, 21372147.

75. Collings PJ and Hird M, Introduction to Liquid Crystals: Chemistry and Physics, Taylor & Francis, 1997.

76. Warner M and Terentjev EM, Liquid Crystal Elastomers, Oxford Science Publications, 2003.

77. Galbraith CG, Skalak R and Chien S, Cell Motility and the Cytoskeleton, 1998, 40, 317–330. [PubMed: 9712262]

78. Markwald RR, Fitzharris TP, Bolender DL and Bernanke DH, Developmental Biology, 1979, 69, 634–654. [PubMed: 437356]

79. Stark H and Ventzki D, Physical Rexlew E, 2001, 64, 031711.

80. Stenull O and Lubensky TC, Physical Rexlew E, 2004, 69, 051801.

81. Miesowicz M, Nature, 1946, 158, 27–27.

82. Skarp K, Lagerwall ST and Stebler B, Molecular Ctystals and Liquid Crystals, 1980, 60, 215–236.

83. Belyaev VV, Physics-Uspekhi, 2001, 44, 255–284.

84. Pelletier V, Gal N, Fournier P and Kilfoil ML, Physical Review Letters, 2009, 102, 188303. [PubMed: 19518917]

85. Ruhwandl RW and Terentjev EM, Physical Rexlew E, 1996, 54, 5204–5210.

86. Schmidt FG, Hinner B and Sackmann E, Physical Review E, 2000, 61, 5646–5653.

87. Frank FC, Discussions of the Faraday Society, 1958, 19–28.

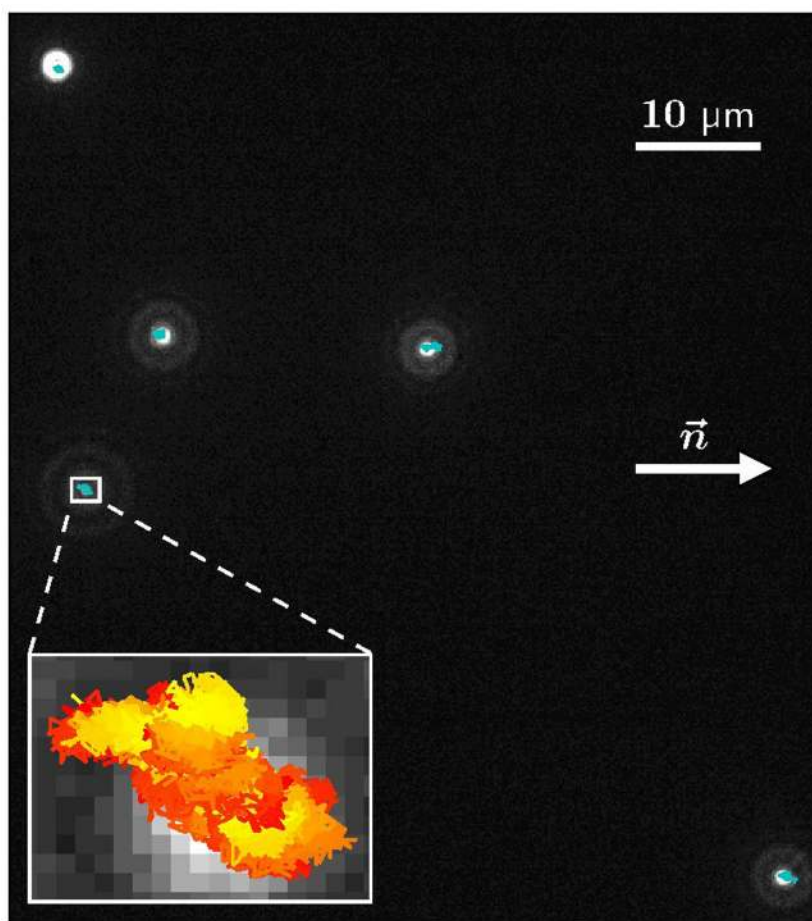88. Stark H and Lubensky TC, Physical Rexlew E, 2003, 67, 061709.
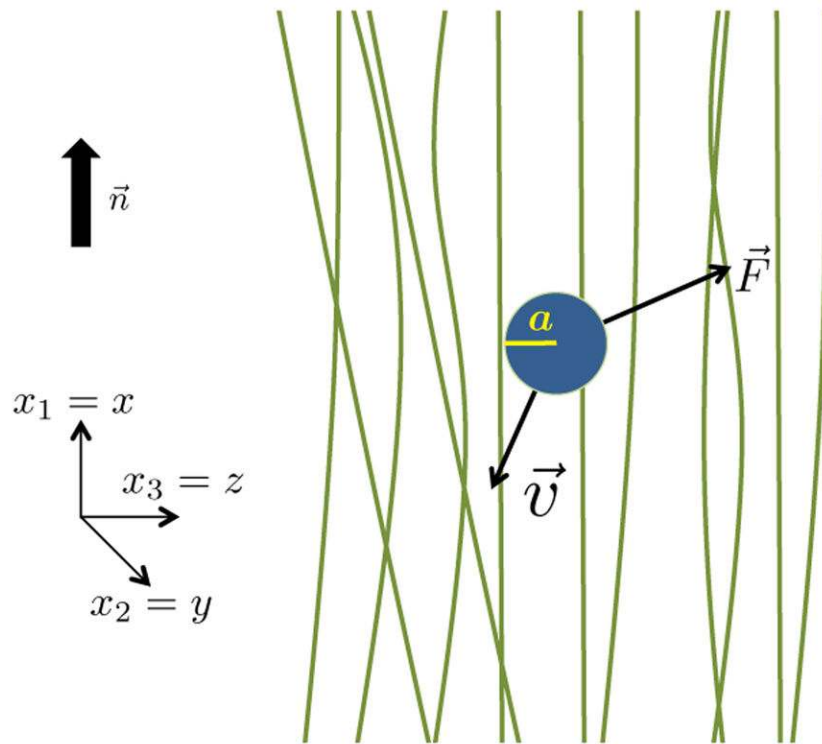
Fig. 1.

Particle of radius a embedded in a nematic complex fluid with director $\vec{n}$. The particle moves with velocity $\vec{v}$ and experiences a resistance force $\vec{F}$.
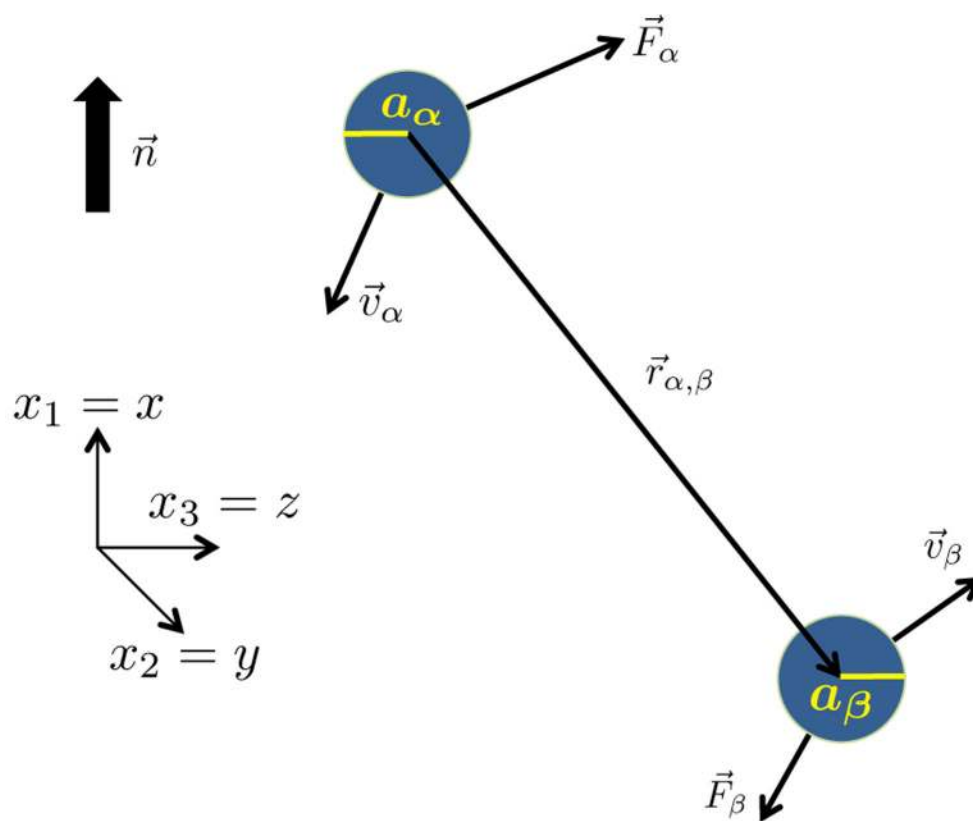
Fig. 2.
Hydrodynamic interaction between two particles separated by a vector $\vec{r}_{\alpha,\beta}$.
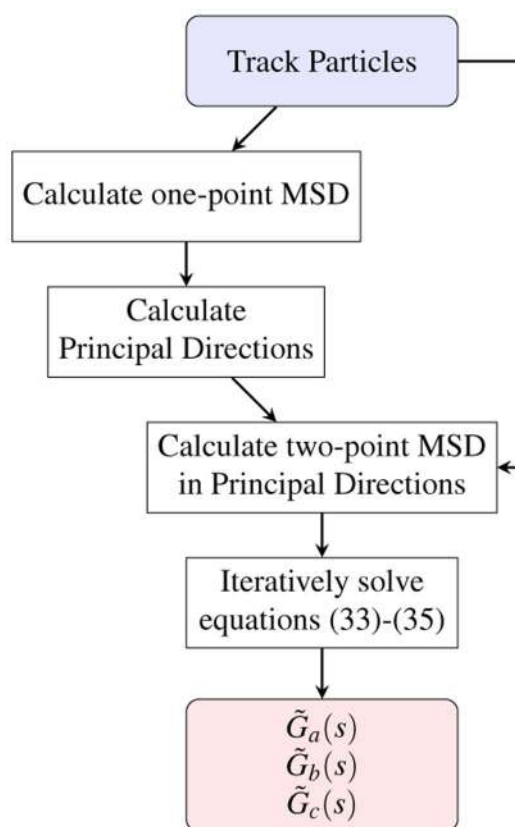
Fig. 3.
Flow diagram summarizing the D2PTM analysis procedures.

Fig. 4.
Fluorescence images of the microparticles embedded in a nematic F-actin fluid with their trajectories superimposed. The inset represents a zoom in one of the particles. It's trajectory is plotted with a color change every 100 time points to highlight both its high- and low-frequency characteristics. The nematic of the fluid is parallel to the horizontal axis.
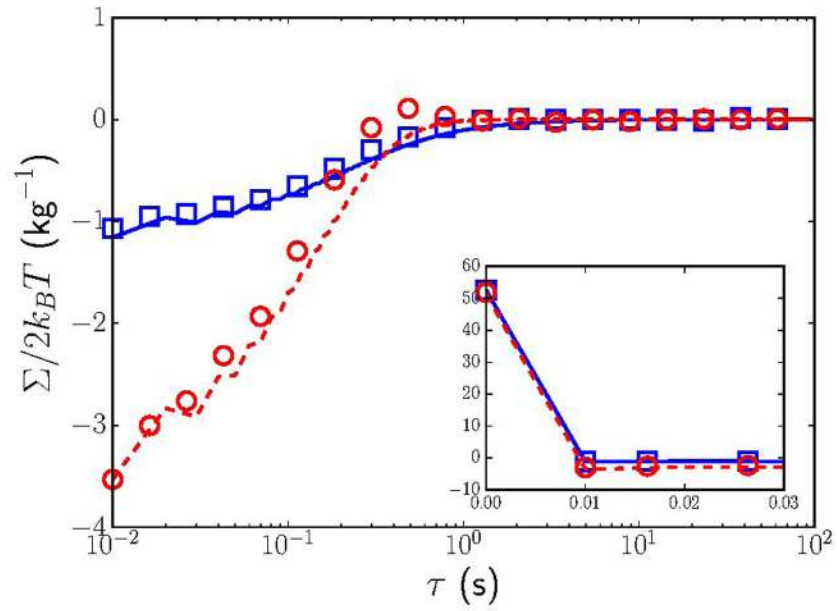
Fig. 5.
Symbols: averaged autocorrelation of the ∥ (□) and ⊥ (○) velocity components of the simulated particles, represented as a function of time separation τ. Lines: covariance kernels $\Sigma_\parallel$ (——) and $\Sigma_\perp$ (– – –) (equations 39–40), represented as a function of the time separation. The vicinity of $\tau = 0$ is shown in the inset.
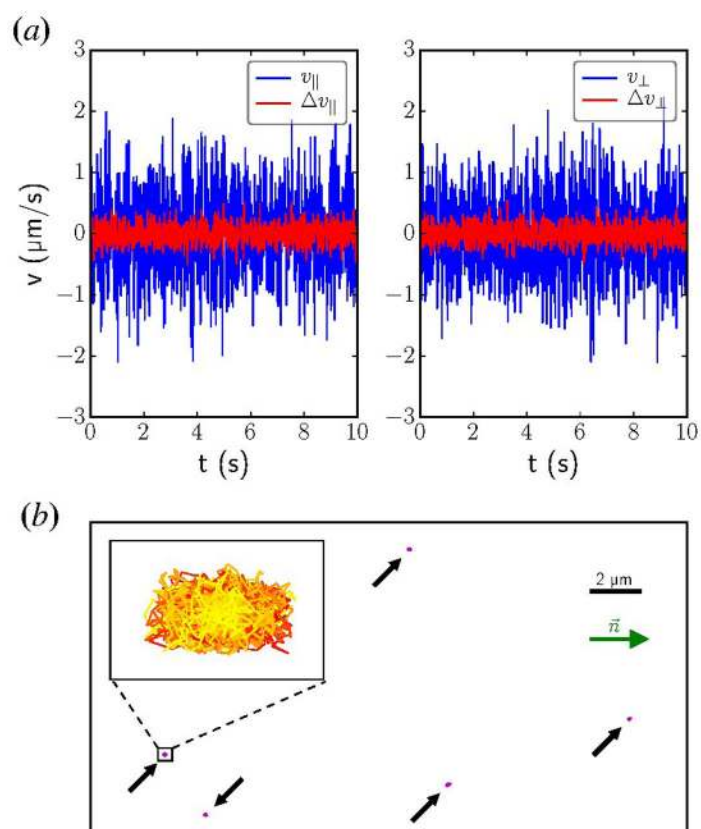
Fig. 6.

(*a*) ∥ and ⊥ velocity components of the simulated Brownian motion of an example simulated particle moving through a nematic Kelvin-Voigt fluid with $\mu_a = 0.5$ Pa, $\mu_b = 0.01$ Pa, $\mu_c = 1$ Pa and $\eta_a = \eta_b = \eta_c = 0.1$ Pa·s. The total velocity is shown in blue (——) while the velocity contribution from hydrodynamic interactions is shown in red (——). (*b*) Trajectories of a representative numerical simulation containing five interacting particles. The nematic is aligned in the horizontal direction. For reference, each trajectory is marked with a black arrow. The inset zooms in the trajectory of one of the particles.
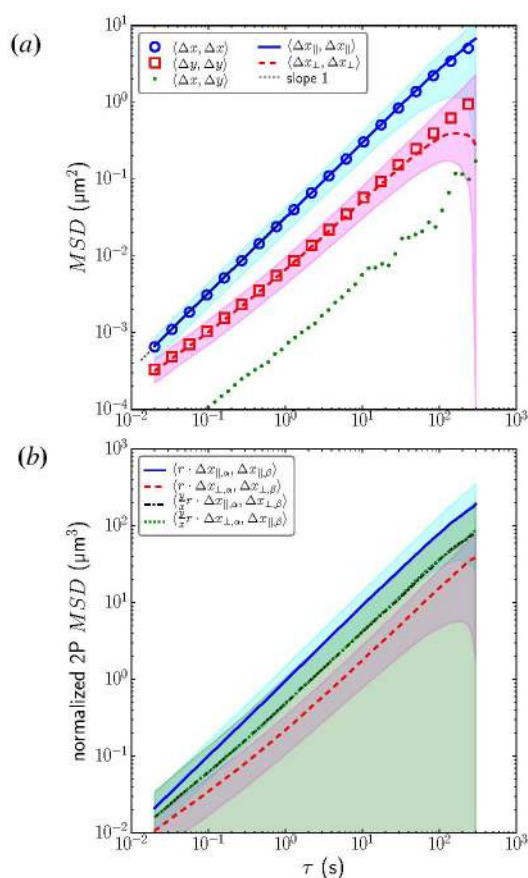
Fig. 7.
(*a*) Experimental one-point MSD of $N = 717$ particles suspended in a 16 wt% nematic DSCG solution. Symbols: MSD along the direction of the capillary tube axis x ($\circ$) and the perpendicular direction y ($\square$). Lines: MSD along the principal directions of maximal ($\parallel$, ——) and minimal ($\perp$, $---$) particle mobility. The dotted green line ($\bullet\bullet\bullet$) represents the $\parallel$-$\perp$ cross-correlation of the particle displacements. For reference, a line with unit slope has been included (--------). (*b*) Renormalized two-point MSD for $M = 3315$ particle pairs in the same DSCG nematic solutions: $\langle r \cdot \Delta x_{\parallel,\alpha}, \Delta x_{\parallel,\beta} \rangle$ (——), $\langle r \cdot \Delta x_{\perp,\alpha}, \Delta x_{\perp,\beta} \rangle$ ($---$), $\left\langle \frac{y}{x} r \cdot \Delta x_{\parallel,\alpha}, \Delta x_{\perp,\beta} \right\rangle$ (— - —) and $\left\langle \frac{y}{x} r \cdot \Delta x_{\perp,\alpha}, \Delta x_{\parallel,\beta} \right\rangle$ (........). The data are plotted versus the time separation τ. The regions between the average MSD plus and minus one standard deviation are shaded, for each direction, in a corresponding color.
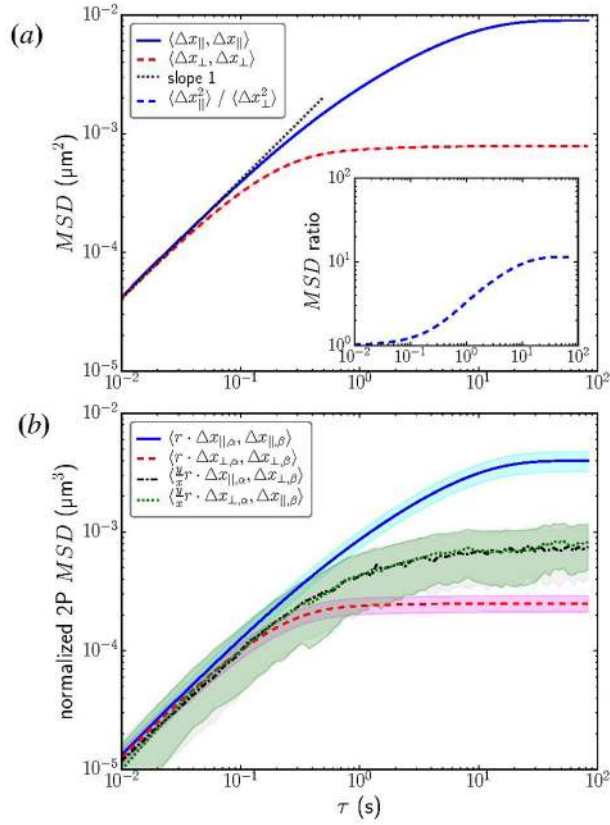
Fig. 8.

(*a*) One-point MSD of $N = 1,000$ simulated particle trajectories in the principal directions of a nematic Kelvin-Voigt fluid with $\mu_a = 0.5$ Pa, $\mu_b = 0.01$ Pa, $\mu_c = 1$ Pa and $\eta_a = \eta_b = \eta_c = 0.1$ Pa·s, projected along the $\parallel$ (———) and $\perp$ (— — —) directions. A line of unit slope is plotted as reference (--------). The inset shows the MSD ratio, $\langle \Delta x_\parallel, \Delta x_\parallel \rangle / \langle \Delta x_\perp, \Delta x_\perp \rangle$. (*b*) Renormalized two-point cross-MSD of the same simulated trajectories ($M = 2,000$ particle pairs): $\langle r \cdot \Delta x_{\parallel,a}, \Delta x_{\parallel,\beta} \rangle$ (———), $\langle r \cdot \Delta x_{\perp,a}, \Delta x_{\perp,\beta} \rangle$ (— — —), $\left\langle \frac{y}{x} r \cdot \Delta x_{\parallel,\alpha}, \Delta x_{\perp,\beta} \right\rangle$ (— · —) and $\left\langle \frac{y}{x} r \cdot \Delta x_{\perp,\alpha}, \Delta x_{\parallel,\beta} \right\rangle$ (·······). The data are plotted versus the time separation τ. The regions between the average MSD plus and minus one standard deviation are shaded, for each direction, in a corresponding color.
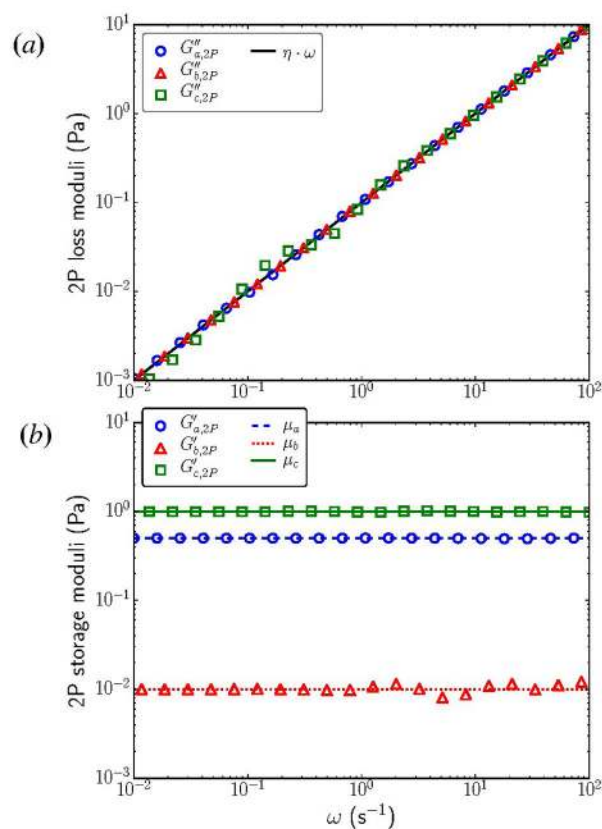
Fig. 9.
(*a*) Symbols: Miesowicz loss moduli recovered by applying D2PTM analysis on simulated particle trajectories; G_a'' (○), G_b'' (△) and G_c'' (□). Solid line: prescribed loss moduli of the material; $\omega\eta_a = \omega\eta_b = \omega\eta_c$ (———). (*b*) Symbols: Miesowicz storage moduli recovered by applying D2PTM analysis on simulated particle trajectories; G_a' (○), G_b' (△) and G_c' (□). Lines: prescribed storage moduli of the material; μ_a (———), μ_b (········) and μ_c (———). The data are plotted versus the frequency ω.
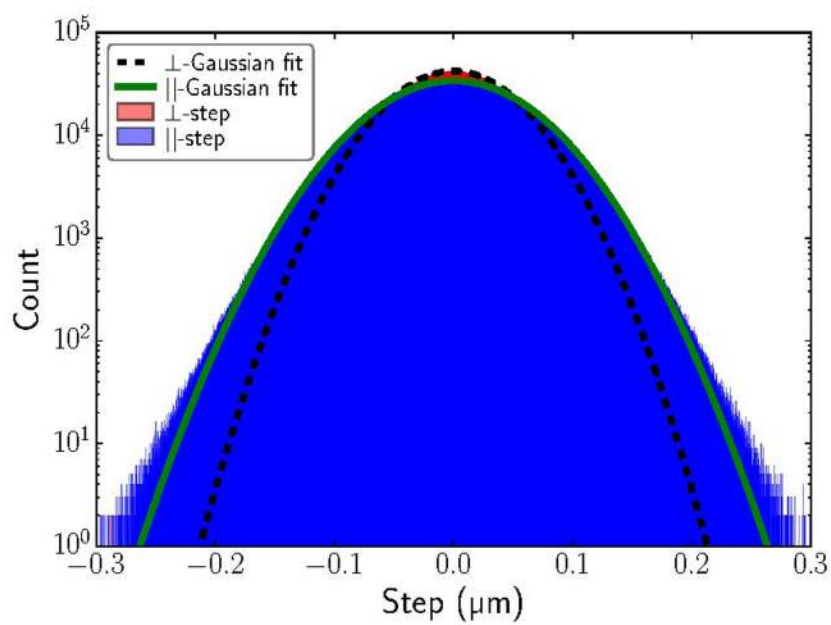
Fig. 10.

Histograms of the experimental particle jumps in the ∥ and ⊥ directions for $\tau = \delta t = 0.02$ s. Two Normal histograms with the same average and standard deviation than the ∥ (— — —) and ⊥ (——) experimental distributions are included for reference.
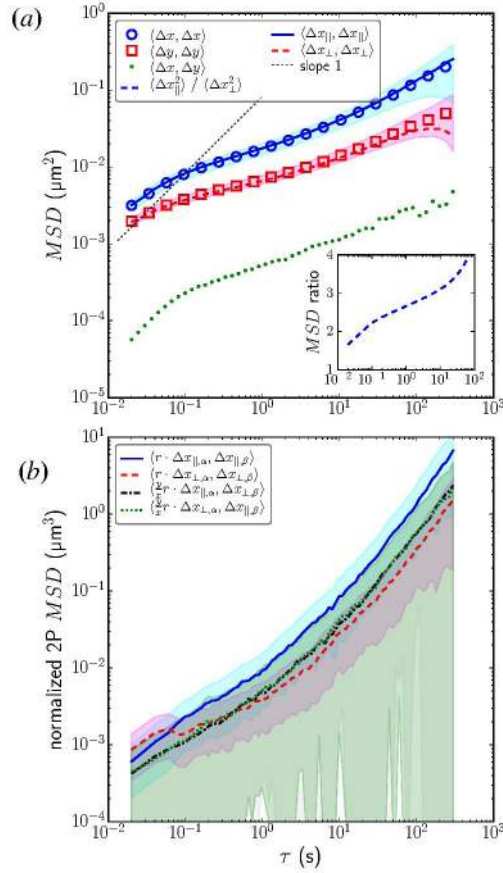
Fig. 11.
(*a*) Experimental one-point MSD of $N = 2,346$ particles embedded in the F-actin nematic solutions. Symbols: MSD along the direction of the capillary tube axis x (○) and the perpendicular direction y (□). Lines: MSD along the principal directions of maximal (∥, ——) and minimal (⊥, – – –) particle mobility. The dotted green line (•••) represents the ∥-⊥ cross-correlation of the particle displacements. For reference, a line with unit slope has been included (--------). The inset shows the MSD ratio $\langle \Delta x_\parallel, \Delta x_\parallel \rangle / \langle \Delta x_\perp, \Delta x_\perp \rangle$. (*b*) Renormalized two-point MSD for $M = 6,105$ particle pairs in the same F-actin nematic solutions: $\langle r \cdot \Delta x_{\parallel,\alpha}, \Delta x_{\parallel,\beta} \rangle$ (——), $\langle r \cdot \Delta x_{\perp,\alpha}, \Delta x_{\perp,\beta} \rangle$ (– – –), $\langle \frac{y}{x} r \cdot \Delta x_{\parallel,\alpha}, \Delta x_{\perp,\beta} \rangle$ (— - —) and $\langle \frac{y}{x} r \cdot \Delta x_{\perp,\alpha}, \Delta x_{\parallel,\beta} \rangle$ (·······). The data are plotted versus the time separation τ. The regions between the average MSD plus and minus one standard deviation are shaded, for each direction, in a corresponding color.
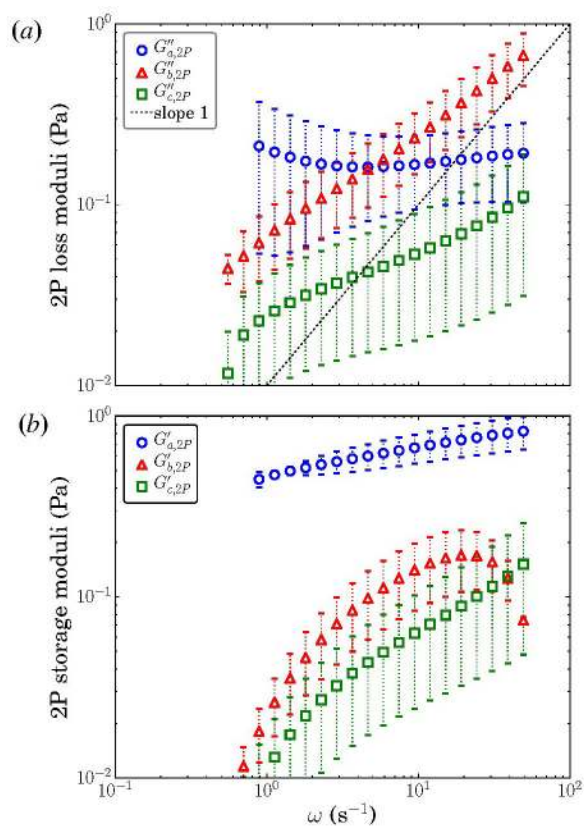
Fig. 12.
(*a*) Directional loss moduli of the F-actin gel. *i.e.* G''_a (○), G''_b (△) and G''_c (□). calculated with the two-particle data. (*b*) Directional storage moduli of the simulated material, *i.e.* G'_a (○), G'_b (△) and G'_c (□), calculated with the two-particle data. The standard deviation is indicated for each frequency.
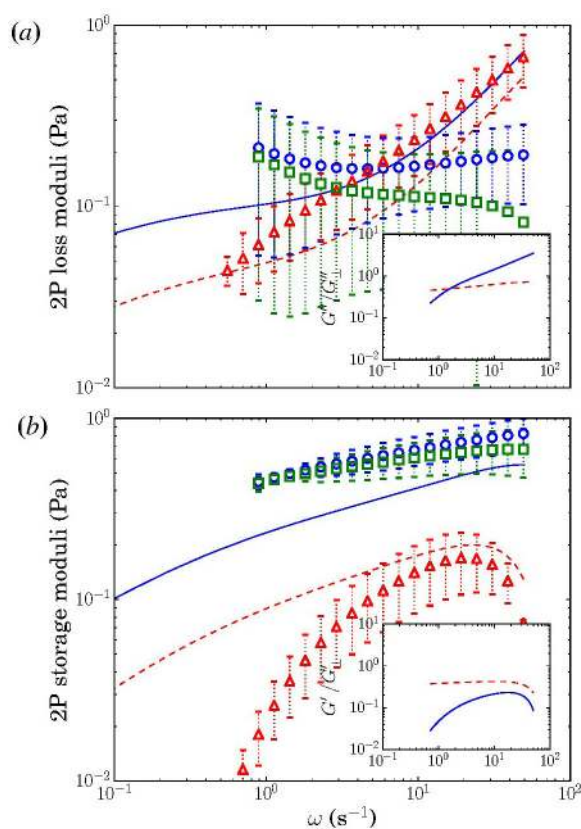
Fig. 13.

Comparison of the directional shear moduli of the nematic F-actin gel calculated with D2PTM and the effective directional shear moduli predicted from one-point PTM. (*a*) Symbols: loss moduli $G''_\perp = G''_a$ (○), $G''_\parallel = G''_b$ (△), $-G''_\Delta = -(G''_c - G''_a)$ (□). Lines: effective loss moduli $G''_{\text{eff}, \perp}$ (——), $G''_{\text{eff}, \parallel}$ (———). Inset: ratio $G''_\parallel / G''_\perp$ (——) and $G''_{\text{eff}, \parallel} / G''_{\text{eff}, \perp}$ (———). (*b*) Symbols: storage moduli $G'_\perp = G'_a$ (○), $G'_\parallel = G'_b$ (△), $-G'_\Delta = -(G'_c - G''_a)$ (□). Lines: effective storage moduli $G'_{\text{eff}, \perp}$ (——), $G'_{\text{eff}, \parallel}$ (———). Inset: ratio $G'_\parallel / G'_\perp$ (——) and $G'_{\text{eff}, \parallel} / G'_{\text{eff}, \perp}$ (———).
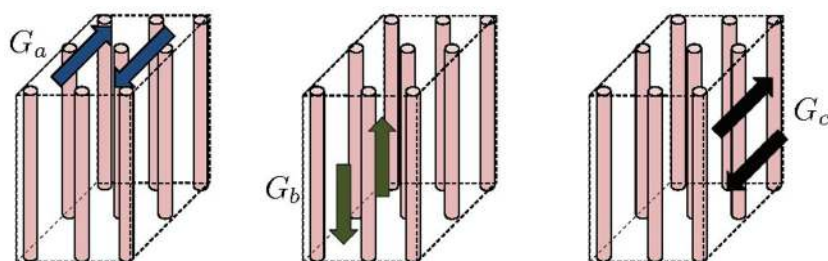
Fig. 14.

Graphical interpretation of the three Miesowicz coefficients in a nematic complex fluid. The direction of the nematic director $\vec{n}$ is represented by red bars. For a uniform shear flow along $\vec{n}$, $\tilde{G}_a$, is excited if $\vec{n}$ is perpendicular to both the flow velocity and its gradient (left panel). $\tilde{G}_b$ is excited if $\vec{n}$ is parallel to the flow (middle panel), whereas $\tilde{G}_c$ is excited if $\vec{n}$ is parallel to the velocity gradient (right panel).
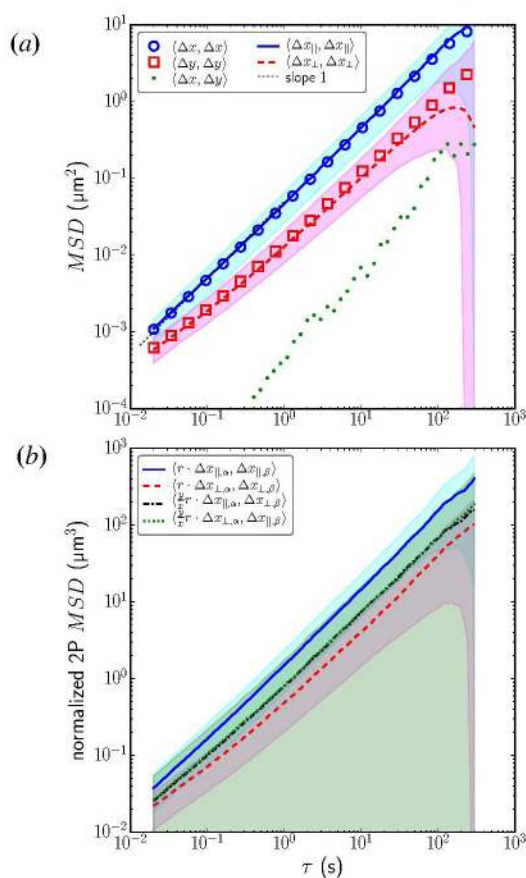
Fig. 15.

(*a*) Experimental one-point MSD of $N = 284$ particles suspended in a 14 wt% nematic DSCG solution. Symbols: MSD along the direction of the capillary tube axis x ($\circ$) and the perpendicular direction y ($\square$). Lines: MSD along the principal directions of maximal ($\parallel$, ——) and minimal ($\perp$, – – –) particle mobility. The dotted green line ($\bullet\bullet\bullet$) represents the $\parallel$-$\perp$ cross-correlation of the particle displacements. For reference, a line with unit slope has been included (--------). (*b*) Renormalized two-point MSD for $M = 816$ particle pairs in the same DSCG nematic solutions: $\langle r \Delta x_{\parallel,\alpha}, \Delta x_{\parallel,\beta} \rangle$ (——), $\langle r \cdot \Delta x_{\perp,\beta}, \Delta x_{\perp,\beta} \rangle$ (– – –), $\left\langle \frac{y}{x} r \cdot \Delta x_{\parallel,\alpha}, \Delta x_{\perp,\beta} \right\rangle$ (— · —) and $\left\langle \frac{y}{x} r \cdot \Delta x_{\perp,\alpha}, \Delta x_{\parallel,\beta} \right\rangle$ (········). The data are plotted versus the time separation τ. The regions between the average MSD plus and minus one standard deviation are shaded, for each direction, in a corresponding color.
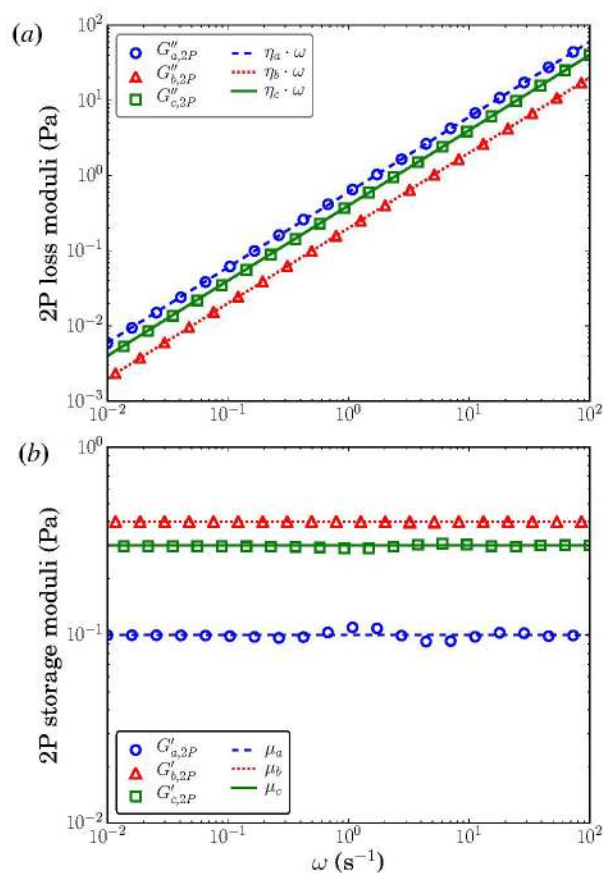
Fig. 16.
(*a*) Directional loss moduli of the simulated material. Symbols: G_a'' ($\circ$), G_b'' ($\triangle$) and G_c' ($\square$) calculated by D2PTM. Lines: actual loss moduli of the material (___, ... and _____).
(*b*) Directional storage moduli of the simulated material. Symbols: G_a' ($\circ$), G_b' ($\triangle$) and G_c' ($\square$), calculated by D2PTM. Lines: actual storage moduli of the material (___, ... and _____).
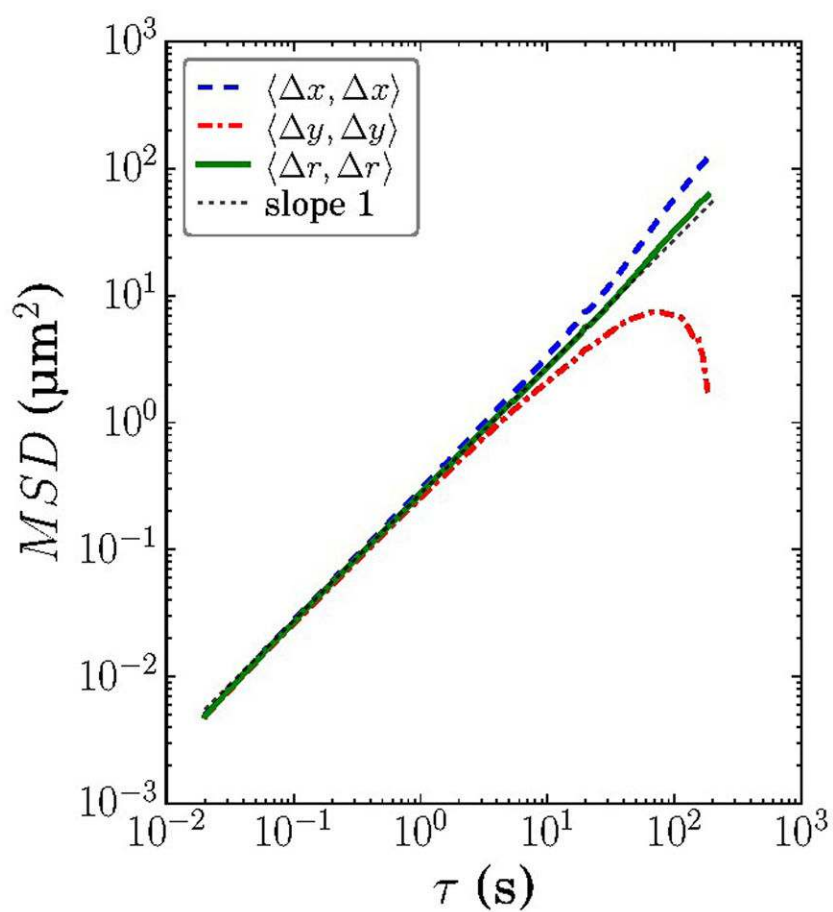
Fig. 17.
MSD of 0.5 μm diameter particles embedded in a 50% (v/v) solution of glycerol in water, plotted as a function of time separation τ. Total (———) MSD as well as MSD in principal directions of maximal (— — —) and minimal (—·—) mobility are shown. A line with unit slope has been included for reference (-------).

Table 1

Miesowicz viscosity coefficients of a 14 wt% and a 16 wt% nematic DSCG solution, as measured by Zhou *el al.* (left column) and by using D2PTM (center column). Effective viscosity coefficients obtained by applying Directional One-Point PTM (right column). All viscosity coefficients were calculated for frequencies around 1 Hz.

(Pa s)	14 wt%		
	Zhou *et al.*	D2PTM	PTM
η_a	n.a.	0.032 ± 0.001	n.a.
η_b	0.008 ± 0.002	0.011 ± 0.002	n.a.
η_c	3.2 ± 0.8	2.0 ± 0.3	n.a.
$\eta_{eff,\parallel}$	n.a.	n.a	0.08 ± 0.005
$\eta_{eff,\perp}$	n.a.	n.a	0.35 ± 0.01

(Pa s)	16 wt%		
	Zhou *et al.*	D2PTM	PTM
η_a	n.a.	0.04 ± 0.02	n.a.
η_b	0.011 ± 0.002	0.015 ± 0.001	n.a.
η_c	20 ± 5	24 ± 2	n.a.
$\eta_{eff,\parallel}$	n.a.	n.a	0.13 ± 0.009
$\eta_{eff,\perp}$	n.a.	n.a	0.8 ± 0.016